Chapter 5

Boundary-induced coupling currents

In this chapter it is shown that spatial distributions in the field-sweep rate $\dot{B}$ *and in the contact resistances* R_a *and* R_c *along the length of a Rutherford-type cable provoke a non-uniform current distribution during and after a field sweep. The process is described by means of Boundary-Induced Coupling Currents (BICCs) flowing through the strands over lengths far larger than the cable pitch. The BICCs are represented by a characteristic length, time and propagation velocity.*

Several longitudinal distributions of $\dot{B}$ *and* R_c *are considered which are present or likely to be present in accelerator magnets. Attention is especially focused on the cable-to-cable connections and the coil ends, where the cable bends around the beam pipe.*

The dependence of the characteristics of the BICCs on the strand resistivity and the contact resistance between strands is calculated.

It is shown that BICCs are always present in coils made of cables with non-insulated strands and it is discussed whether R_c*- or* $\dot{B}$*-variations are the dominant cause.*

The BICCs are evaluated by means of a novel experiment in which a 1.3 m long Rutherford-type cable is exposed to a local field variation. The results clearly demonstrate the existence of BICCs and validate the use of the network model for calculating them.

5.1 Introduction

In chapter 4 the ISCCs are dealt with in the case where the $\dot{B}$-variation along the length of the cable is uniform. However, in all magnets a certain spatial variation of the field is present along the length of the cable and hence a spatial variation of $\dot{B}$ during a field sweep. In this chapter only variations in $\dot{B}_\perp$ (i.e. the field change normal to the large face of the cable, see eq. 4.1) are considered since the magnitude of the interstrand and boundary-induced coupling currents is mainly affected by this component.

As an example, the field change $\dot{B}_\perp$ (in the centre of the cable) along the length z of the cable in a 1 m long LHC dipole magnet is shown in Fig. 5.1 for a central-field-sweep rate of 0.0066Ts^{-1}. Only the cable of the inner coil of one pole, having 13 turns, is shown with a total length of about 25 m (see also Figs. 2.2b and 2.3).

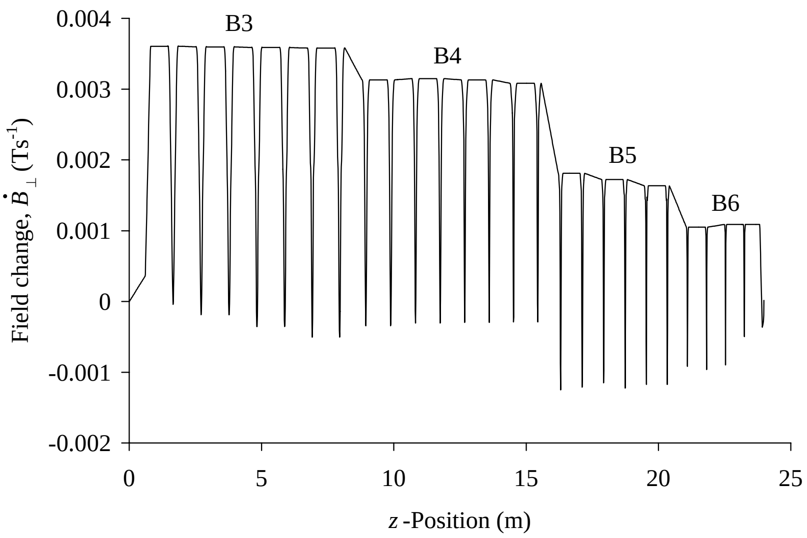

Figure 5.1. The field change $\dot{B}_\perp$ along the length of the cable of the inner coil of one pole of a 1 m long LHC dipole magnet with a 50 mm aperture. The field change is the average field change in the centre of the cable. The central-field-sweep rate is 0.0066 Ts^{-1}. The labels indicate the block numbers (see Fig. 2.2b).

The sharp decreases in $\dot{B}_\perp$ correspond to those parts in the coil where the cable bends around the beam pipe. The position $z=0$ denotes the end of the current lead. Part of the curve (2.1 m$<z<$6.2 m) is enlarged in Fig. 5.2 in which $\dot{B}_\perp$ at three different places across the cable width is depicted versus the scaled axial position of the cable. The spatial $\dot{B}_\perp$-distribution can be separated into two regimes:

- Strong variations for which $|\Delta\dot{B}_\perp/\Delta z|$ is of the same order as $|\dot{B}_{\perp,max}/L_{p,s}|$, with $\Delta\dot{B}_\perp$ the change in $\dot{B}_\perp$ over the longitudinal length Δz and $\dot{B}_{\perp,max}$ the maximum field change. An example is the average $\dot{B}_\perp$-variation between $z=20L_{p,s}$ and $z=21L_{p,s}$ (see Fig. 5.2) where $|\Delta\dot{B}_\perp/\Delta z|=|\dot{B}_{\perp,max}/L_{p,s}|=0.0053/0.13=0.04$ Ts^{-1}m^{-1}.

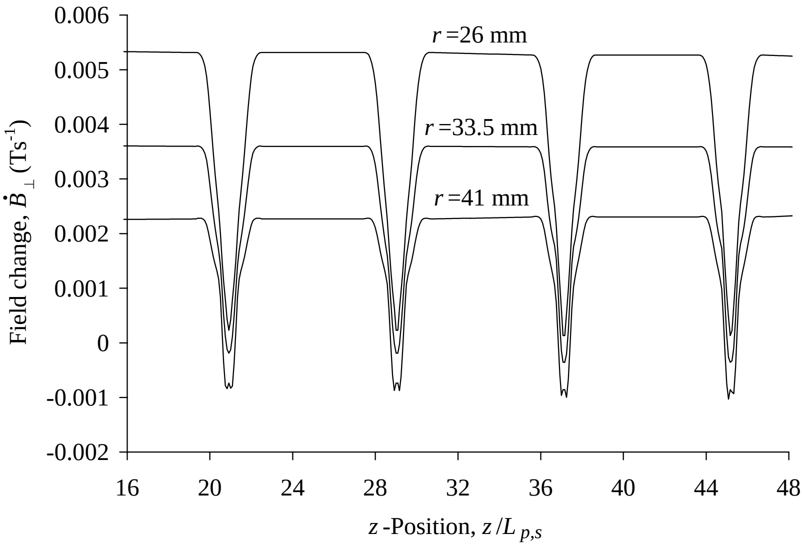

Figure 5.2. The field change $\dot{B}_\perp$ along the scaled length of the cable of a 1 m long LHC dipole magnet with a 50 mm aperture. The field changes at three radii are shown (see Fig. 2.2a) for several turns of block 3 (B3). The central-field-sweep rate is 0.0066 Ts^{-1} and $L_{p,s}$ is equal to 0.13 m.

- Weak variations for which $|\Delta\dot{B}_\perp/\Delta z|$ is much smaller than $|\dot{B}_{\perp,max}/L_{p,s}|$. An example is shown in Fig. 5.1 for the average variation of the field in the entire inner coil of the magnet, where $|\Delta\dot{B}_\perp/\Delta z|=0.0025/24=1\cdot10^{-4}$ Ts^{-1}m^{-1} while $|\dot{B}_{\perp,max}/L_{p,s}|=0.0053/0.13=0.04$ Ts^{-1}m^{-1}.

In accelerator dipole and quadrupole magnets both cases are present whereas, for example, in solenoid magnets mainly weak variations occur.

Besides spatial distributions of $\dot{B}_\perp$ spatial distributions of R_c are also present in an accelerator magnet. In section 4.6 the case of a varying R_c across the cable width was discussed, which is due to the keystone angle and the gradient in the transverse pressure $P_\perp$ across the cable width. However, variations in R_c along the cable length also occur and can be separated in:

- Variations over lengths far larger than $L_{p,s}$ which are present in the entire cable since the transverse pressure varies considerably over the cross-section of the coil. Measurements of the contact resistances, performed on several sections of the inner coil of two SSC dipole model magnets, have shown that the contact resistances could vary by more than one order of magnitude over the turns of one coil [Kovachev, '93a/b,'94].
- Variations over lengths up to a few cable pitches which are present:
  - in the coil ends where the transverse pressure $P_\perp$, that strongly influences R_c, on the cable varies significantly; analysis of the cross-sections of coils has shown that in these parts of the magnet the average contact area between strands reduces to almost zero,
  - in the soldered connections between different cables in the magnet,
  - in local 'shorts' between strands.

Recently, the influence of spatial $\dot{B}_\perp$- and R_c-distributions on the coupling currents in Rutherford-type cables was also treated by Akhmetov et al., showing that the coupling currents I_s and I_c vary periodically with a period equal to the cable pitch [Akhmetov, '93a/'94/'95].

Egorov also concluded that the coupling currents and power can increase substantially due to the axial $\dot{B}_\perp$-variations although, under certain conditions, it can be imperceptible as well [Egorov, '94]. The coupling currents can increase up to magnitudes that, in combination with the transport current, saturate the strand and cause a quench or initiate a current redistribution.

Also Krempasky and Schmidt have recently shown that non-uniform $\dot{B}$-distributions provoke additional coupling currents exhibiting very long time constants [Krempasky, '95a/b]. Their approach was based on the solution of the diffusion equation which they applied to a two-wire configuration coupled through a transverse conductance.

An analytical solution of the decay of current loops as a function of time is given by Akhmetov et al. under weak and strong excitation levels [Akhmetov, '93b]. Computations are made in the case of an SSC dipole magnet, showing that the time constant under weak excitation can be as large as 10^6 s and decreases strongly if the transport current reaches 90% of its critical value.

The above-mentioned approaches demonstrate qualitatively that non-uniformities in the magnetic flux or cross-contact resistances always results in periodically varying coupling currents. In this chapter calculations are performed to investigate the current pattern caused by longitudinal $\dot{B}_\perp$- and R_c-variations more systematically. The calculations are made using the network model of a Rutherford-type cable as described in detail in section 4.2. Additional assumptions which are used in the simulations are given in section 5.3. The current patterns are evaluated by means of a new type of current, the so called '*Boundary-Induced Coupling Current* (BICC)', and illustrated in section 5.4.1. The term 'boundary' indicates that BICCs are generated by geometrical boundaries, boundaries in $\dot{B}$ and internal boundaries such as changes in R_a and mainly R_c. The BICCs differ from the ISCCs with respect to:

- the length over which they flow in the strands, represented by a characteristic length ξ,
- the characteristic time τ_{bi} which they exhibit,
- the propagation velocity v_{bi},
- the magnitude $I_{bi,0}$.

In sections 5.4.1-5.4.4 the results are presented for a straight cable subject to a single '$\dot{B}_\perp$-step', which implies that one part of the cable is exposed to a field variation $\dot{B}_\perp$ while the other part is not. Several formulas are presented by which the characteristic time and length of the BICCs can be estimated. In order to draw conclusions with respect to an entire coil, it is shown in section 5.4.5 how the results of a single $\dot{B}_\perp$-step can be applied to estimate the BICCs in a cable subject to an arbitrary longitudinal $\dot{B}_\perp$-variation.

In section 5.5 special attention is paid to the case of a cable which is partially exposed to a varying field. It is shown that the BICCs can cause a significant enhancement of the coupling power loss. The large characteristic lengths of the BICCs cause the loss to be also dissipated in those parts of the cable which are not exposed to the local $\dot{B}_\perp$. In section 5.6 the case of a cable is investigated with R_c>>R_a simulating, for example, a cable with a resistive barrier between the two layers. In section 5.7 the BICCs are calculated for a cable that is exposed to a uniform $\dot{B}_\perp$ but has a local R_c-variation. The calculations are especially useful for understanding the influence of R_c-variations in the coil ends and cable-to-cable connections on the magnitude of the BICCs.

In section 5.8 a novel measurement set-up is described for investigating the BICCs in a straight Rutherford-type cable, subject to a local $\dot{B}_\perp$, by scanning the magnetic field along the cable length. The experimental results are compared to the calculations in order to understand the pattern of the BICCs and to validate the simulations.

In the next section the case of a cable with insulated strands is briefly discussed, since the current distribution has a certain resemblance to the current distribution as produced by the BICCs.

5.2 Cables with insulated strands

The current in each strand of a multistrand cable with insulated strands is constant through the total length of the cable. The current distribution in the cable subject to a homogeneous field can be easily derived since the current distributes itself among the strands in such a way that the voltages over all the strands of the cable are equal. The voltage over strand *i* consists of a resistive and an inductive part, and is given by:

$$U^i = U_R^i + U_{ind}^i = I_{str}^i \left(R_{ser}^i + \rho_s^i l_{str} / A_{str}\right) + \sum_{j=1}^{N_s} M^{ij} \dot{I}_{str}^j \quad [\mathrm{V}]\,, \tag{5.1}$$

with I_{str} the strand current, R_{ser} the series (or joint) resistance of the transfer length near the current leads, ρ_s the strand resistivity, l_{str} the length of the strand, A_{str} the cross-section of the strand and M^{ij} the mutual inductance between strands *i* and *j*. This analytical approach can be used if the cable (with insulated strands) is subjected to a constant field (change) and is ramped without generating a large self-field compared to the field produced by the other turns. The transfer length consists of:

– the transfer across the copper of the current lead, the solder and the outer copper sheath of the strand (until the outermost layer of filaments),
– the transfer from the outermost layer of filaments to the more inner layers.

In general the first transfer traject is the major contribution to the resistance and the joint resistances can differ by a large amount. Eq. 5.1 shows that, once all the currents are stabilised (so that the inductive term can be disregarded), the current is distributed according to the relative values of the series and strand resistances. Hence, the distribution can strongly depend on:

– the current level because the strands can have a different voltage-current relation,
– the external field since the contact resistances can be magnetoresistive.

The strand currents under DC conditions always differ somewhat as it is impossible to achieve exactly the same soldering [Faivre, ’81].

The contribution of the joint resistance R_{ser} and the strand resistance R_{str} to the total resistance R_{tot} is examined in the case of a dipole magnet. Therefore, both R_{ser} and R_{str} are calculated for the inner coil of a 1 m long PBD magnet (see Table 2.1).

- The joint resistance. The resistance of the soldered connection with length $L_{p,s}$ between two Rutherford-type cables is typically 0.4 nΩ. For a 26-strand cable this implies about 10 nΩ on both ends of the strands, so in total 20 nΩ per strand.
- The strand resistance. Since the field (and hence the critical strand current) varies strongly over the cross-section of a magnet, the strand resistance has to be determined by integration along the total length l_{str} of the strand:

$$R_{str} = \frac{1}{A_{str}} \int_0^{l_{str}} \rho_s^i(I_{tr,str})dz \quad [\Omega] , \tag{5.2}$$

with A_{str} the cross-section of the strand. The power law of the voltage-current relation (see eq. 4.8) is used to describe the current dependence of ρ_s. Fig. 5.3 shows R_{str} as a function of the transport current for several n-values in eq. 4.8 (assuming $\rho_s = 10^{-14}$ Ωm at $I_{tr,str} = I_{C,str}$). In the case of an operation current that is 90% of the critical current the resistance R_{str} is about 10^{-6} to 10^{-1} nΩ for $n = 30$ and $n = 10$ respectively.

At weak excitation levels the current distribution is dominated by the joint resistance whereas only for currents very close to the critical current does the strand resistance have to be taken into account, especially for long magnets made of a cable having a small n-value. Also in the case of cables with non-insulated strands the current distribution under DC conditions will be given by the differences in joint resistances among the strands.

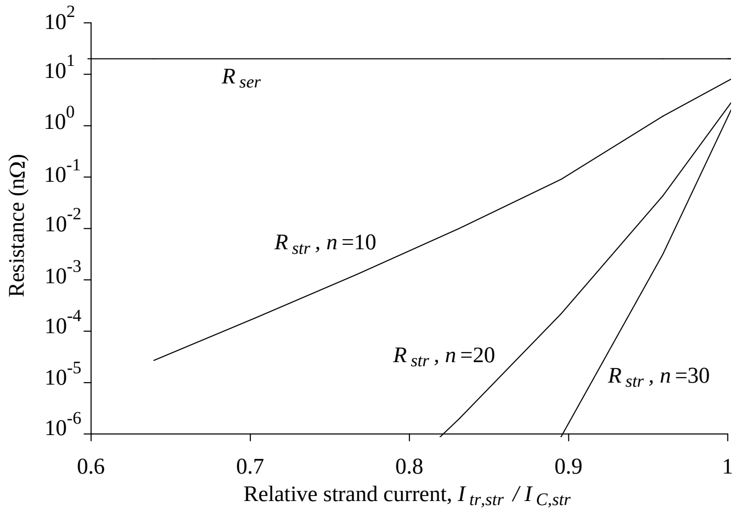

Figure 5.3. The resistance of the strands of an inner coil of a 1 m long LHC-type dipole magnet as a function of the scaled transport current for several n-values. R_{str} is almost proportional to the length of the magnet. The series resistance of 20 nΩ, corresponding to two cable-to-cable connections of 0.4 nΩ, is independent of the magnet length.

By changing the cable current, the strand currents will change according to their relative self- and mutual inductances. In the case of fully transposed cables, in which each strand has the same self- and mutual inductances with the other strands, the ramping of the total current will not affect the differences between the strand currents already created under DC conditions, if of course R_{ser} and ρ_s remain constant. In practice, however, a change of the current also causes a change of the field, and the strand resistivity can increase significantly due to the dynamic resistivity (see eq. 3.6):

$$\rho_{dyn} = \frac{A_{str}}{I_{tr,str}} E_{dyn} = \frac{d_f d_s^2}{3 I_{C,str}(B,T)} \dot{B}_{\perp s} \quad [\Omega\text{m}] , \tag{5.3}$$

with $\dot{B}_{\perp s}$ the field change normal to the strand axis (disregarding the small twist angle of the filaments). The dynamic resistivity can easily be larger than the resistivity ρ_s under DC conditions. For example, $\rho_{dyn}=10^{-15}$ Ωm at $\dot{B}_{\perp s}=0.1$ Ts^{-1} (for $d_f=10$ μm, $d_s=1.3$ mm and $I_{C,str}=1000$ A), while $\rho_s=10^{-16}$ Ωm at $I_{tr,str}=0.8 I_{C,str}$ (for $n=20$ and $\rho_s=10^{-14}$ Ωm at $I_{tr,str}=I_{C,str}$). In a coil each strand of the cable has an almost equal dynamic resistivity, so that a field-sweep will not cause differences between the strand currents due to different ρ_{dyn}.

Considering non-fully transposed cables (for example a 6 around 1 cable configuration), differences between the self- and the mutual inductances are present. During a current ramp, some strands will carry more current than others which can significantly decrease the quench current of such a cable if used in AC applications, see for example [Schermer, '79], [Faivre, '81], [Knoopers, '85]. These time constants of the (re)distribution process of the currents depend on the series and strand resistances and on the self- and mutual inductances. The time constants are therefore current-dependent since R_{ser} is magnetoresistive and R_{str} is strongly current-dependent.

The current distribution in non-fully transposed cables is not further discussed since all the strands of a Rutherford-type cable have almost the same length. Small differences in the lengths of less than 0.1% can be present due to, especially, the coil ends but they hardly affect the current distribution.

5.3 Simulating BICCs

The network model, as extensively described in section 4.2, is used to calculate the BICCs in a Rutherford-type cable. The longitudinal coordinate of the cable is denoted by z. The cable lengths from $z=0$ to the ends of the cable are referred to as $l_{cab,1}$, for $z<0$, and $l_{cab,2}$, for $z>0$ (see Fig. 5.4). The end of the cable is either the physical end (with or without a cable-to-cable connection) or a part where the strands are in the normal state (and hence have a relatively large strand resistivity).

Throughout the chapter the *strand sections* are denoted by the *strand position* (see Fig. 5.5) which is independent of the longitudinal position, while the (physical) *strands* are denoted by the *strand number* i. So, each strand will subsequently pass through all the strand positions.

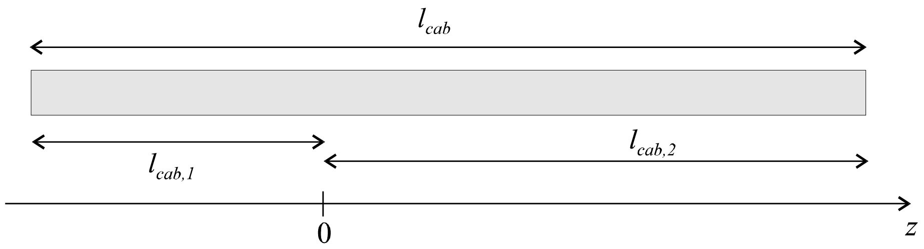

Figure 5.4. Definition of the lengths in a cable.

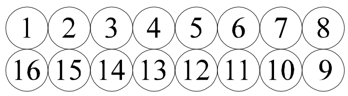

Figure 5.5. Numbering of the strand positions in the cross-section of a 16-strand Rutherford-type cable.

At $z=k{\cdot}L_{p,s}$ (with k an integer), the strand numbers correspond to the strand position numbers. Hence, at $z=0$, strand 1 bends around the edge of the cable while at $z=L_{p,s}/4$ strand 1 is located near the centre of the cable.

The calculations are performed assuming that:

– The strands in the cable have the same length. This implies that all strands have the same self-inductance, whereas the values of the mutual inductance depend on the relative position of the strands in the cable.
– The strands have the same series resistances R_{ser}.
– The strand currents are smaller than the critical current ($I_{str}<I_{C,str}$, i.e. the strands are not saturated) and the strand resistivity ρ_s is the same for all the strands and is assumed to be independent of the current in the strand. In the network model the strand resistivity is included by means of a resistance R_s between two nodes as given by eq. 4.11.
– A non-uniform current distribution within the strand (due to persistent currents and interfilament coupling currents) is not taken into account.
– Only the field change $\dot{B}_\perp$ is considered because the field changes $\dot{B}_\|$ and $\dot{B}_z$ (see Fig. 4.1) turn out to have a much smaller effect. At a first approximation, the ratio of the magnitudes of the BICCs for $\dot{B}_\perp$ and $\dot{B}_\|$ is equal to the ratio of the magnitudes of the ISCCs for $\dot{B}_\perp$ and $\dot{B}_\|$ (see eq. 4.20).
– The contact resistance R_a between adjacent strands is much larger than the contact resistance R_c between crossing strands ($R_a>>R_c$). Only section 5.6 deals with the specific case where $R_a<<R_c$, simulating the presence of a resistive barrier between the two layers of the cable.
– In the ends of the cable the distribution of the ISCCs is given by the solution for a cable without longitudinal non-uniformities that is exposed to the local $\dot{B}$, which leads to the solutions obtained in section 4.4.1. Other boundary conditions, however, do not influence the results from a qualitative point of view.

The assumptions imply that the transport current is uniformly distributed among the strands. In the following the term ‘steady-state’ denotes the condition that the cable is exposed to a certain $\dot{B}_\perp$-distribution for a time much larger than all characteristic times involved.

Most of the simulations are performed by subsequently changing all the parameters in the network model, namely h, w, $L_{p,s}$, N_s, R_c, R_a, $\dot{B}_\perp$ and ρ_s. The results are presented as analytical formulas that describe the dependence of the currents, time constants and decay lengths on the above-mentioned parameters. Therefore, each analytical relation contains one or more constants of proportionality that are needed to fit the numerical results to the analytical expressions.

Many simulations and, in particular, step-response calculations require a large-size matrix as shown in section 4.2. To reduce the computing time, the simulations are often performed on cables with only 8 or 10 strands. Also a large strand resistivity is used in order to decrease the length over which the BICCs decay (see section 5.4.2) and hence the matrix size. Extrapolation to cables with more strands and a small strand resistivity could therefore result in less accurate solutions. The estimated error in the constants of proportionality are given for each analytical expression.

5.4 Cables exposed to a $\dot{B}_\perp$-step

The characteristic BICC distribution in a cable is illustrated in section 5.4.1 by means of a step increase in $\dot{B}_\perp$ along the length of the cable. The magnitude of the BICCs as well as the characteristic length ξ are dealt with in section 5.4.2, the characteristic time τ_{bi} in section 5.4.3 and the propagation velocity of the BICCs in section 5.4.4.

In section 5.4.5 it is shown how the solution of the BICCs for an arbitrary $\dot{B}_\perp$-distribution can be obtained by considering it as a superposition of $\dot{B}_\perp$-steps. Specific longitudinal variations, which are likely to occur in a magnet, such as:

– $\dot{B}_\perp$ which linearly increases from 0 to a certain value, simulating that part of a magnet where the cable enters the magnet,
– $\dot{B}_\perp$ which is small over a certain length of the cable, simulating the coil ends, where the cable bends around the beam pipe,

can be treated by this approach. Field variations across the cable width only slightly change the distribution of the ISCCs (see section 4.7) but do not generate BICCs, and are therefore not dealt with in this chapter.

5.4.1 Characteristic BICC pattern

A 16-strand cable is considered (with $R_c = 1$ μΩ, $R_a = 10$ μΩ, $d_s = 1.3$ mm and $L_{p,s} = 100$ mm) which is exposed to a field change $\dot{B}_\perp$ of 0 for $z < 0$ and 0.01 Ts^{-1} for $z \geq 0$. The transport current $I_{tr,str}$ in the strands is equal to 20 A.

The characteristic coupling-current pattern in the cable is illustrated by means of the current in a given strand as well as the current at a given strand position. Fig. 5.6 depicts the current in two *strands* (numbers 2 and 12).

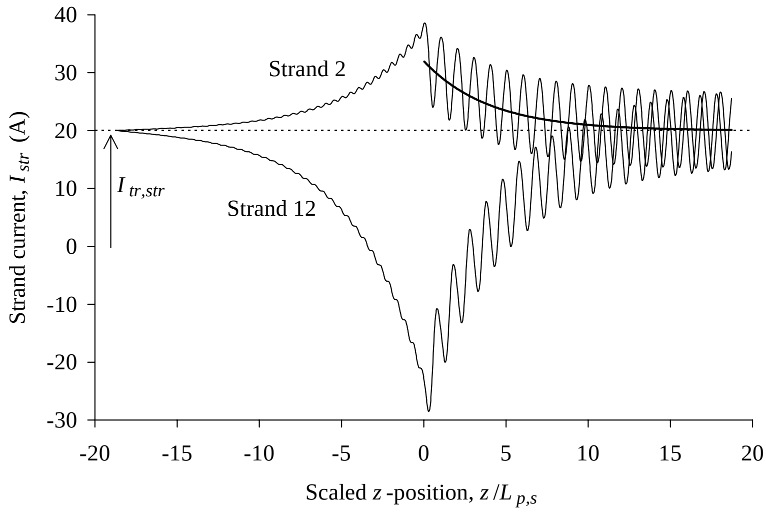

Figure 5.6. The characteristic pattern of the strand currents in two strands of a Rutherford-type cable subject to field changes of 0 for $z<0$ and 0.01 Ts^{-1} for $z\geq 0$ (Regime A: $\rho_s = 2\cdot 10^{-14}$ Ωm). The transport current is shown by a dotted line. The bold line shows the transport current and the BICC in strand 2 for $z\geq 0$.

The strand current can be regarded as a superposition of three components:

- The transport current which is equal to 20 A all along the strand.
- The oscillating term, with an average equal to 0, related to the ISCCs which are mainly present for $z\geq 0$. The maximum ISCC is about 7 A and corresponds to the ISCC for a cable without longitudinal variations (see eq. 4.20). The amplitude of the ISCC pattern remains constant for $z\geq 0$.
- The BICC which is maximum close to the $\dot{B}_\perp$-step and decays quasi-exponentially for $z<0$ as well as $z\geq 0$ with a characteristic length ξ, which is equal for all the strands. The magnitude of the BICCs can be different for $z<0$ and $z\geq 0$, as shown in Fig. 5.6 where the bold line represents the current in strand 2 corrected for the ISCC contribution. The difference depends on the strand number and its maximum is equal to the maximum value of the ISCCs.

Fig. 5.7 depicts the same strand currents but now when ρ_s is much smaller. The contribution of the ISCCs remains the same. The BICCs, however, decay quasi-linearly towards zero instead of quasi-exponentially and their magnitude is much larger than in the previous case.

Two regimes can be distinguished:

Regime A. The BICCs decay quasi-exponentially along the length and approach 0 clearly before the end of the cable. In this case a characteristic length ξ of the BICCs can be defined as the length over which the BICCs decay to 1/e of their initial value. The length of the cable is at least several times ξ and the boundary conditions at the ends of the cable do not influence the magnitude and the decay length of the BICCs.

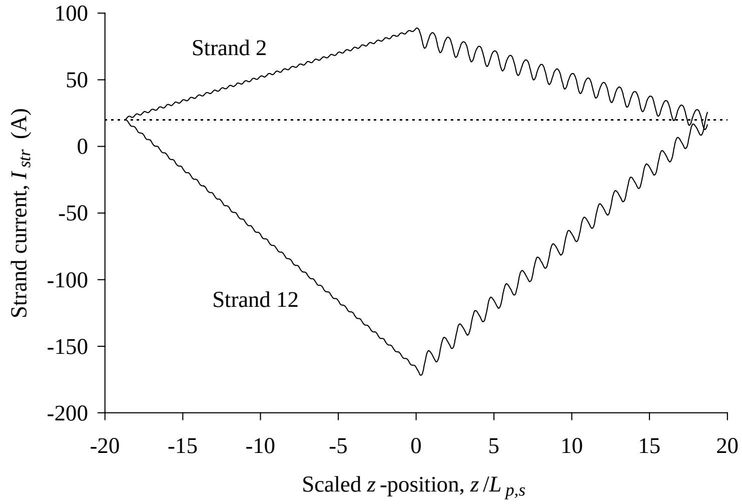

Figure 5.7. The characteristic pattern of the strand currents in two strands of a Rutherford-type cable subject to field changes of 0 for $z<0$ and 0.01 Ts^{-1} for $z\geq 0$ (Regime B: $\rho_s=2\cdot 10^{-17}$ Ωm). The transport current is shown by a dotted line.

Regime B. The BICCs decay quasi-linearly towards the boundary values at the end of the cable, which therefore influence the decay. In general the boundary conditions impose that the BICCs are 0 at the ends of the cable. Different boundary conditions, however, will give a qualitatively similar behaviour but quantitatively different results.

The intermediate regime, where the decay of the BICCs is somewhere in-between an exponential and a linear one, is not dealt with in this chapter. An estimate of the characteristics of the BICCs can be obtained by assuming a linear decay. In section 5.4.2 the parameters are discussed that define whether the BICCs decay quasi-exponentially or quasi-linearly.

In order to illustrate the current distribution in the cable more clearly, the strand current at a given *strand position* will now be analysed under the same conditions as applied in Figs. 5.6 and 5.7. The strand current at the edge of the cable (position 1, see Fig. 5.5) is depicted in Figs. 5.8 and 5.9 for regimes A and B. Fig. 5.10 shows an enlargement of Fig. 5.8 for $-2L_{p,s}<z<2L_{p,s}$ for two strand positions.

The average strand current at the edge is equal to $I_{tr,str}=20$ A for $z<0$ and is about 13 A for $z\geq 0$ which corresponds to the sum of $I_{tr,str}$ and the ISCC (of about -7 A) for a cable without longitudinal variations shown as a bold line in Fig. 5.8. Hence, the strand current at a given *strand position* can be regarded as a superposition of:

– the transport current,
– an oscillating part from the BICCs,
– the ISCCs of which the value depends on the strand position (see, for example, Fig. 4.6). This can be seen in Fig. 5.10 where the ISCC is about -7 A at position 1 while it is about 0 at position 5.

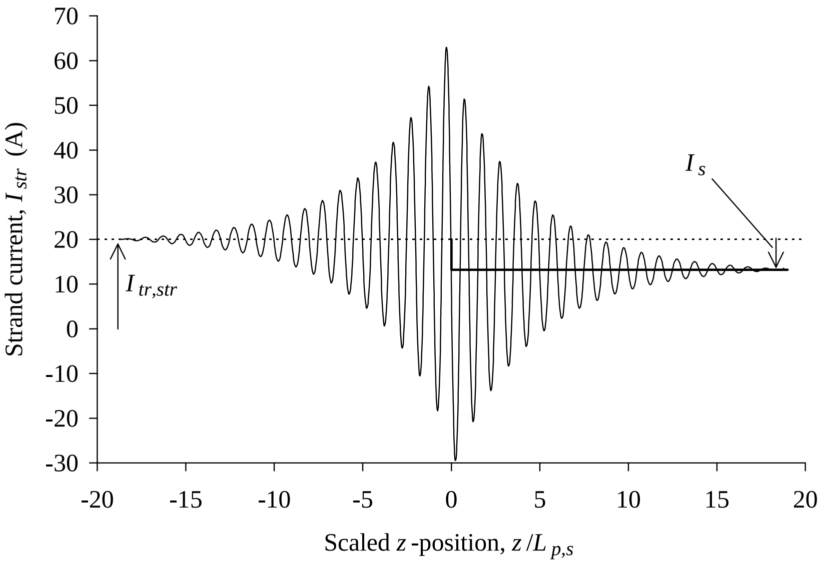

Figure 5.8. The characteristic pattern of the strand current at *position* 1 of a Rutherford-type cable subject to field changes of 0 for $z<0$ and 0.01 Ts^{-1} for $z\geq 0$ (Regime A: $\rho_s = 2\cdot 10^{-14}$ Ωm). The transport current is shown by a dotted line, and the ISCC by a bold line.

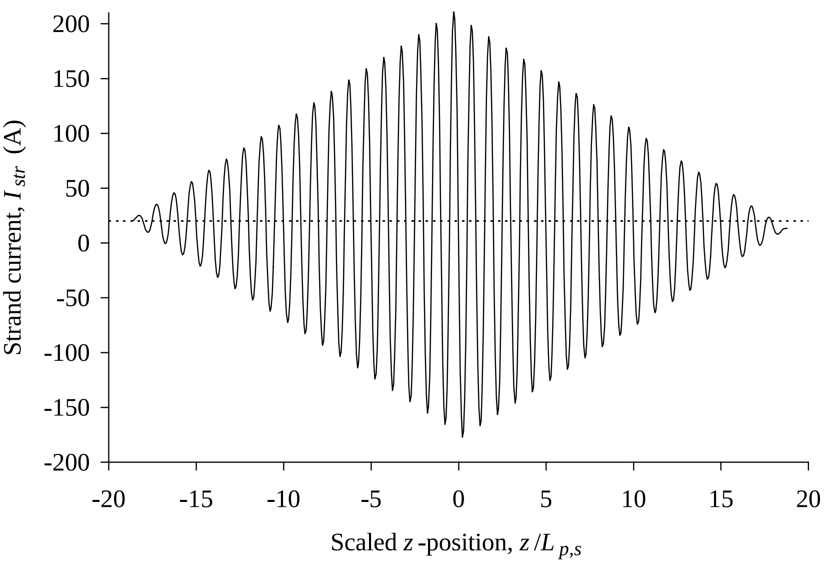

Figure 5.9. The characteristic pattern of the strand current at *position* 1 of a Rutherford-type cable subject to field changes of 0 for $z<0$ and 0.01 Ts^{-1} for $z\geq 0$ (Regime B: $\rho_s = 2\cdot 10^{-17}$ Ωm). The transport current is shown by a dotted line.

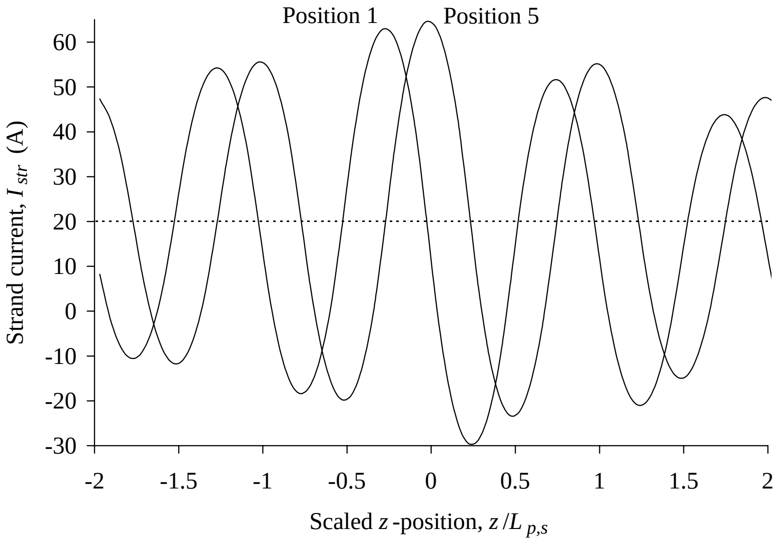

Figure 5.10. The characteristic pattern of the strand current at *positions* 1 and 5 of a 16-strand Rutherford-type cable subject to field changes of 0 for $z<0$ and 0.01 Ts^{-1} for $z\geq 0$ (Regime A: $\rho_s = 2\cdot 10^{-14}$ Ωm). The transport current is shown by a dotted line.

If the transport currents in the strands are not equal, an additional variation of the current at a given strand position is present.

A regular pattern exists in the magnitudes of the BICCs. In each cross-section of the cable opposite strands (for example 3 and 11 or 7 and 15, see Fig. 5.5) carry BICCs with the same magnitude but with an opposite sign. Adjacent strands have only slightly different BICCs as shown in Fig. 5.11. For $z=0$ the maximum BICCs occur in the centre of the cable i.e. at positions $N_s/4$ and $3N_s/4$.

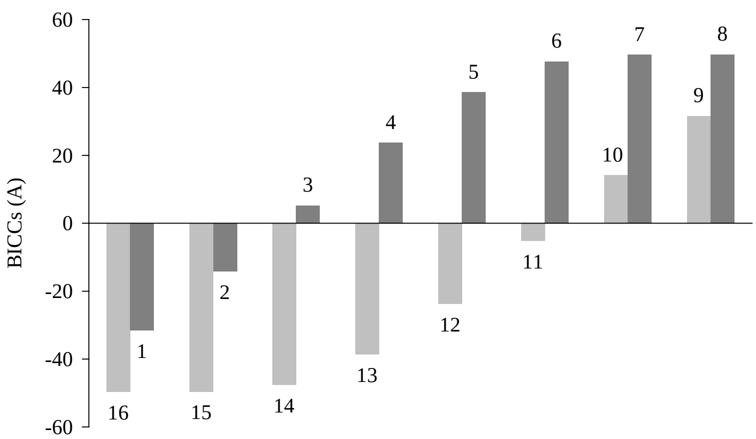

Figure 5.11. Illustration of the magnitude of the BICCs in a 16-strand cable at a certain z-position. The labels indicate the strand positions as given in Fig. 5.5.

The regular pattern is typical for BICCs and causes them to generate more pronounced field errors than in the case of a random current distribution among the strands, such as that caused by different joint resistances. The magnitudes of the BICCs change mainly due to cross-over currents I_c flowing between the upper (positions 1 to $N_s/2$) and lower layers (positions $N_s/2+1$ to N_s) through the contact resistances R_c. The currents in R_a contribute only slightly to the magnitude of the BICCs (for $R_a \geq R_c$). Hence, the currents I_c correspond to the change in the current I_{str} in the axial direction of the strand (see Figs. 5.6 and 5.7). This implies that the strands carrying large BICCs are more heated than the strands carrying small BICCs, which in turn results in a periodic behaviour of I_c and, therefore, the coupling power P_c along the cable length.

It is important that the the decay of the BICCs along the length is only quasi-exponential or quasi-linear if the R_c is constant. In the case of a cable with a longitudinal R_c-variation, the change of the BICCs along the cable length will vary according to the local R_c. This implies that, for example, the slope dI_{bi}/dz of the linear decay shown in Fig. 5.7 will not be constant along the length but will locally increase (decrease) in sections with smaller (larger) R_c. This will be discussed in more detail in section 5.8.3.

In Fig. 5.12 the coupling power loss is shown in the entire cable for regimes A and B. At each z-position the power loss is calculated by the individual losses in each contact summed over all the (N_s-1) contacts in one band (see Fig. 4.2). The values are then divided by the length of one band ($=L_{p,s}/N_s$) to obtain the local power loss per unit length of cable.

In the case of constant $\dot{B}_\perp$ and R_c along the cable length the cross-over currents I_c are z-independent and result in a constant power loss P_c of 0 for $z<0$ and $2.21 \cdot 10^{-3}$ Wm^{-1} for $z \geq 0$ (see eq. 4.17), shown as a dotted line in Fig. 5.12. The BICCs enhance the ISCL since the average power loss is larger than 0 for $z<0$ and larger than $2.21 \cdot 10^{-3}$ Wm^{-1} for $z \geq 0$.

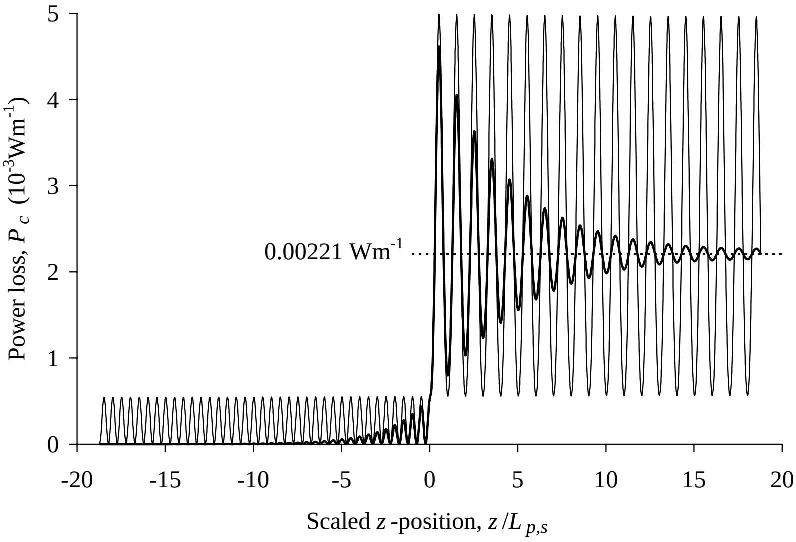

Figure 5.12. The characteristic pattern of the ISCL in a Rutherford-type cable subject to field changes of 0 for $z<0$ and 0.01 Ts^{-1} for $z \geq 0$. Bold line: $\rho_s = 2 \cdot 10^{-14}$ Ωm, regime A. Normal line: $\rho_s = 2 \cdot 10^{-17}$ Ωm, regime B.

The increase is more pronounced if the magnitude of the BICCs is larger, so that the enhancement of the power loss is larger for regime B than regime A. Note that for regime B the amplitude of the P_c-variations remains constant on both sides of the $\dot{B}_{\perp}$-step while the amplitude decreases for regime A. The reason for this is that the maximum dI_{str}/dz per twist pitch, which is related to the amplitude of the P_c-variations, remains constant for regime B while it decreases for regime A (see Figs. 5.6 and 5.7).

It is interesting to see that for regime B the maximum ISCL for $z<0$ corresponds to the minimum ISCL for $z\geq 0$. The same holds for regime A close to $z=0$. This implies that for $z\geq 0$ the mean currents through R_c (in one band) due to a constant $\dot{B}_{\perp}$ are twice as large as those due to the $\dot{B}_{\perp}$-step. The maximum local ISCL for $z\geq 0$ is therefore $(3/2)^2=2.25$ times larger than the ISCL without $\dot{B}_{\perp}$-step. For $z<0$ the maximum local ISCL is $(1/2)^2=0.25$ times the ISCL (at $z\geq 0$) without $\dot{B}_{\perp}$-step. The enhancement of the ISCL due to a $\dot{B}_{\perp}$-step is discussed in more detail in section 5.5.

In Fig. 5.13 the coupling power loss in each resistance R_c is shown for regime A for $3L_{p,s}<z<6L_{p,s}$. A periodic pattern (with period $L_{p,s}$) is present where parts having large and small local power losses alternate.

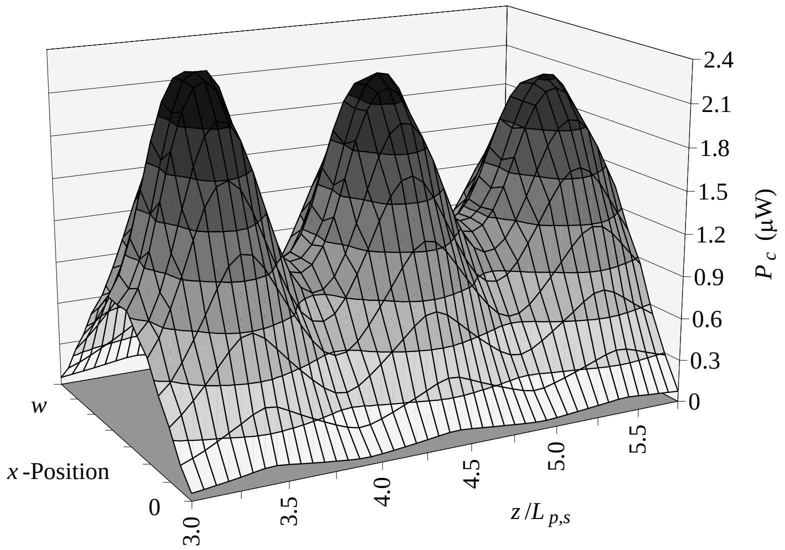

Figure 5.13. The characteristic pattern of the ISCL across the cable width (with $w=10.4$ mm) of a Rutherford-type cable subject to field changes of 0 for $z<0$ and 0.01 Ts^{-1} for $z\geq 0$ (Regime A: $\rho_s=2\cdot 10^{-14}$ Ωm).

Half of the strands are less heated than the average since they ‘slalom’ in between the hot spots. These strands correspond to those with small BICCs. The other half of the strands, which carry large BICCs, are heated more than the average. Hence, the spots with a large local power loss correspond to those areas where strands with large BICCs cross each other.

Although the power loss fluctuates strongly, this does not imply that the actual temperature of the strands fluctuates to the same extent. Due to the good thermal conductivity inside the cable the temperature will probably be quite uniform under normal operating conditions in an accelerator magnet.

5.4.2 Magnitude and characteristic length of BICCs under steady-state conditions

The following analytical relations for ξ and $I_{bi,max}$ in regimes A and B are derived by a fit to the numerical calculations. The errors in the fitting constants are about 5-10%. The calculations are performed for $8 \le N_s \le 40$. For larger N_s the simulations become too time-consuming. However, the relations probably also hold for cables with $N_s > 40$ although the indicated errors could increase by a factor 2.

Regime A.

The BICC in strand i (see for example Fig. 5.6) can be approximated by (neglecting the small periodic signal for $z < 0$):

$$I_{bi,i}(z) = I_{bi,0} \sin(2\pi(i-0.5)/N_s) e^{-|z|/\xi} \quad \text{[A]} , \tag{5.4}$$

where $I_{bi,0}$ is defined as the average between the maximum magnitude of the BICCs at positive and negative z-positions and is given by:

$$I_{bi,0} = 0.88 \frac{w\xi}{R_c}\left(1 - e^{-N_s/9.6}\right)\Delta\dot{B}_\perp \quad \text{[A]} . \tag{5.5}$$

The relation can be expressed as a function of the maximum ISCC, $I_{s,max}$, by combining eqs. 5.5 and 4.20, assuming $\cos(\pi x/w) = 1$ and $\Delta\dot{B}_\perp = \dot{B}_\perp$:

$$I_{bi,0} = 21 \frac{\xi}{L_{p,s} N_s}\left(1 - e^{-N_s/9.6}\right) I_{s,max} \quad \text{[A]} . \tag{5.6}$$

The impact of these relations for practical cables is discussed later. The characteristic length ξ is equal for all the strands in the cable and is given by:

$$\xi = 0.50 \frac{L_{p,s}}{N_s} \sqrt{R_c / R_s} \quad \text{[m]} . \tag{5.7}$$

For $R_s = 0$ the BICCs have to be calculated using the formulas for regime B. The length ξ can be expressed in terms of ρ_s by combining eqs. 4.11 and 5.7:

$$\xi = 0.50 \sqrt{\frac{R_c L_{p,s} \pi d_s^2}{2 \rho_s N_s}} \quad \text{[m]} . \tag{5.8}$$

The relation is shown in Fig. 5.14 for several resistivities. ξ can be large for practical superconductors especially for small ρ_s and large R_c. It is important that ρ_s denotes an *effective* strand resistivity that the BICCs 'see' which could be different from the strand resistivity that the transport current 'sees'. A brief discussion and an estimate of this effective resistivity is given in section 7.7.5. Note that in the case of normal conducting strands with a large resistivity, ξ is very small so that, in fact, no BICCs are present.

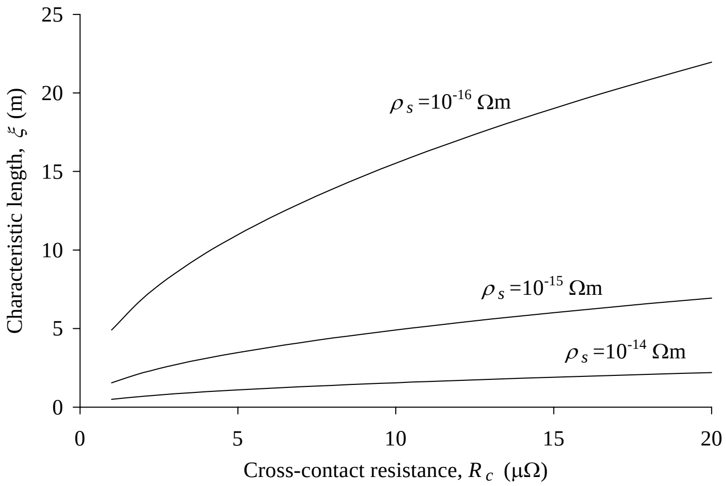

Figure 5.14. Calculated characteristic lengths ξ of a 26-strand Rutherford-type cable with $d_s = 1.3$ mm and $L_{p,s} = 0.1$ m.

If ξ is much larger than the lengths $l_{cab,1}$ (for $z<0$) and $l_{cab,2}$ (for $z\geq 0$) then the BICCs have to be calculated using the formulas for regime B. If ξ is of the same order as $l_{cab,1}$ (or $l_{cab,2}$) then the exact BICC pattern cannot be described by simple analytical relations but the relations for regime A or B can be used as a first approximation.

Regime B.

A similar expression for $I_{bi,0}$ is obtained as eq. 5.4 with the difference being that the BICCs depend linearly on the cable length:

$$I_{bi,i}(z) = I_{bi,0} \sin\left(2\pi(i-0.5)/N_s\right)\left(1-|z|/l_{cab,i}\right) \quad [\text{A}] , \tag{5.9}$$

with $l_{cab,i}=l_{cab,1}$ for $z<0$ and $l_{cab,i}=l_{cab,2}$ for $z\geq 0$. The maximum magnitude of the BICCs in the cross-section of the cable equals:

$$I_{bi,0} = 1.0 \frac{w l_{cab,eff}}{R_c}\left(1-e^{-N_s/9.6}\right)\Delta\dot{B}_{\perp} \quad [\text{A}] , \tag{5.10}$$

with:

$$l_{cab,eff} = 2\frac{l_{cab,1} l_{cab,2}}{l_{cab,1}+l_{cab,2}} \quad [\text{m}] . \tag{5.11}$$

Again, the current $I_{bi,0}$ can be written as as a function of $I_{s,max}$, by combining eqs. 5.10 and 4.20, assuming $\cos(\pi x/w)=1$ and $\Delta\dot{B}_{\perp}=\dot{B}_{\perp}$:

$$I_{bi,0}=25\frac{l_{cab,eff}}{L_{p,s}N_s}\left(1-e^{-N_s/9.6}\right)I_{s,max} \quad [\mathrm{A}]\,. \tag{5.12}$$

The maximum magnitude $I_{bi,0}$ of the BICCs for practical cables (i.e. N_s is about 20-40) is, in first approximation, about a factor $\xi/L_{p,s}$ (regime A, see eq. 5.6) or $l_{cab,eff}/L_{p,s}$ (regime B, see eq. 5.12) larger than the maximum ISCC. This factor explains the large difference in the magnitude of the BICCs shown in Figs. 5.8 (with $I_{bi,0}\approx 50$ A) and 5.9 (with $I_{bi,0}\approx 200$ A) since $l_{cab,eff}\approx 4\xi$ for the given simulation parameters.

The impact of the BICCs becomes clear by considering a dipole coil, where $\Delta\dot{B}_{\perp}\approx\dot{B}_{\perp}$ in the coil ends (see Fig. 5.1). For large ξ (regime A) or $l_{cab,eff}$ (regime B) the BICCs can attain very large values, even at small field-sweep rates and large contact resistances. For example, $I_{bi,0}=92$ A for $N_s=26$, $w=0.017$ m, $\xi=10$ m, $R_c=10$ μΩ and $\Delta\dot{B}_{\perp}=0.0066$ Ts^{-1} (regime A).

Note that the magnitude of the BICCs is proportional to $\dot{B}_{\perp}$, provided that ξ (for regime A) is independent of $\dot{B}_{\perp}$. This is an important conclusion that is used in chapter 7 in order to distinguish the field distortions caused by the BICCs and those caused by a non-uniform current distribution among the strands (due to different joint resistances).

Although the magnitude of the BICCs varies considerably between regimes A and B, the maximum in the local power loss is the same (see Fig. 5.12), because the slope dI_{str}/dz is the same for $z\to 0$, and therefore also the local currents I_c for $z\to 0$.

In this section a constant R_c along the cable is assumed. However, as discussed in the introduction of this chapter, spatial R_c-variations are always present in a coil. The BICCs caused by these variations are discussed in section 5.7 in the case of a constant $\dot{B}_{\perp}$. However, spatial R_c-distributions also change the magnitude of BICCs provoked by a $\dot{B}_{\perp}$-step. In general the local increase of the BICCs, i.e. dI_{bi}/dz, (see for example Figs. 5.6 and 5.7) is inversely proportional to the local R_c. This means that all the sections in a cable having a small R_c could enhance the magnitude of the BICCs, even if these sections are placed in a low-field region of the magnet. A typical example is the joint between the cables of two poles. An example of the influence of a local decrease in R_c on the magnitude of the BICCs is given in section 5.8.3. Expressions for all typical R_c- and $\dot{B}_{\perp}$-variations along the cable length cannot be given since the number of combinations is much too large.

The BICCs can only attain the steady-state values if:

– the total current (i.e. the sum of the transport current, the ISCC and the BICC) in each strand section remains smaller than the critical current,
– the characteristic time of the BICCs is smaller than the time during which the cable is exposed to a field change. In the next section the characteristic time of the BICCs is discussed by means of their step response.

5.4.3 Characteristic time of BICCs

The development of the BICCs in time is investigated by introducing self- and mutual inductances between the strands as discussed in section 4.2. As an example, the decay of the BICCs in an 8-strand cable (with $d_s = 1$ mm, $\rho_s = 1.2 \cdot 10^{-14}$ Ωm and $L_{p,s} = 0.1$ m) is calculated for:

$t \leq 0$: $\dot{B}_\perp = 0$ for $z < 0$ and $\dot{B}_\perp = 0.01$ Ts^{-1} for $z \geq 0$,
$t > 0$: $\dot{B}_\perp = 0$ for $z < 0$ and $\dot{B}_\perp = 0$ for $z \geq 0$.

At $t = 0$ the BICCs have attained their steady-state values and decay quasi-exponentially along the length (see eq. 5.4). For $t > 0$ the BICCs decay to 0, starting from the initial value at $t = 0$, as illustrated in Fig. 5.15, where the decay of the BICCs at several z-positions is depicted as a function of the time. The moment at which the BICCs start to decay propagates through the cable. Near $z = 0$ the decay is instantaneous, whereas for larger z the decay starts after a certain time. This propagation is discussed in section 5.4.4.

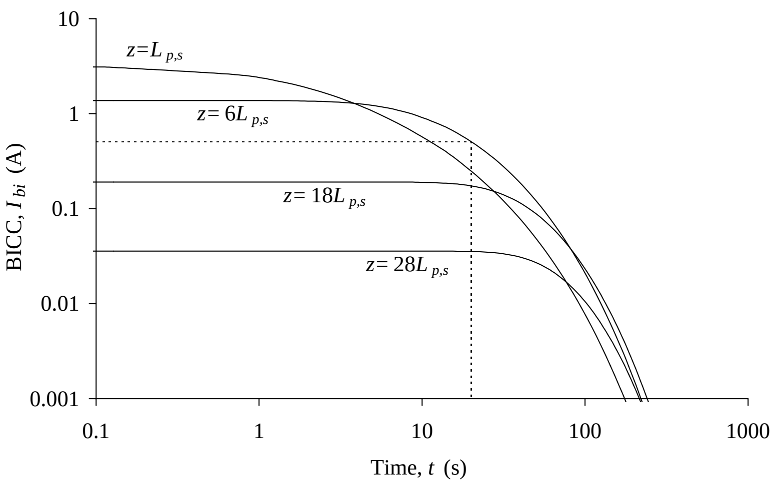

Figure 5.15. The decay of the BICC in a given strand as a function of the time at several z-positions. The dotted line shows the characteristic time at $z = 6L_{p,s}$ i.e. the period during which the BICC at $z = 6L_{p,s}$ has decayed to 1/e of its initial value.

The relative decay is identical for all the strands. Since the decay as a function of the time is not exponential, the following *characteristic* times are defined:

– $\tau_{bi}(z)$: The time during which the BICCs at position z decay to 1/e of their initial values (see section 5.4.4).
– $\tau_{bi,av}$: The time during which the average of the absolute value of all the BICCs in the whole cable decays to 1/e of its initial value.

The characteristic times are calculated for both regimes with the same approach as used for the calculation of $\tau_{is,cab}$ (see section 4.4.2), i.e. in the case of a straight cable having strands with a round cross-section. The characteristic times increase slightly for cables with a small keystone angle or highly compressed cables. The results of the numerical calculations are expressed by analytical relations which are valid for $8 \le N_s \le 40$ with an error in the constants of proportionality of about 20%.

Regime A.

The characteristic time $\tau_{bi,av}$ satisfies:

$$\tau_{bi,av} = 2.4 \cdot 10^{-8} \frac{L_{p,s}}{R_s} = 1.2 \cdot 10^{-8} \frac{N_s \pi d_s^2}{\rho_s} \quad [\mathrm{s}]\ , \tag{5.13}$$

where the constants have the dimensions $\Omega \mathrm{sm}^{-1}$. If $\rho_s = 0$ the BICCs should be calculated using the formulas for regime B so that eq. 5.13 is no longer relevant. The times $\tau_{bi,av}$ are about 30% larger than the times $\tau_{bi}(0)$.

Eq. 5.13 shows that $\tau_{bi,av}$ is independent of R_c, which can be understood by considering the cable as a simple *LR*-circuit, where L represents the effective inductance of the strands over a length ξ and R represents the effective resistance of the parallel connected resistances R_c. Hence, L is linear in ξ and R is linear in R_c/ξ. Since the time constant of an *LR*-circuit is given by $\tau = L/R$, the time constant $\tau_{bi,av}$ is proportional to $\xi/(R_c/\xi) = \xi^2/R_c$. This implies that $\tau_{bi,av}$ is independent of R_c, because ξ^2 is linear in R_c (see eq. 5.7).

Regime B.

Since the BICCs decay linearly towards the end of the cable, the time constant $\tau_{bi,av}$ is now related to the lengths $l_{cab,1}$ and $l_{cab,2}$ and can be expressed by:

$$\tau_{bi,av} = 6.2 \cdot 10^{-8} \frac{l_{cab,1} l_{cab,2} N_s^2}{L_{p,s} R_c} \quad [\mathrm{s}]\ , \tag{5.14}$$

where the constants has the dimension $\Omega \mathrm{sm}^{-1}$. The characteristic time $\tau_{bi,av}$ can be expressed as a function of the interstrand time constant of a single cable by combining eqs. 5.14 and 4.31:

$$\tau_{bi,av} = 3.8 \frac{l_{cab,1} l_{cab,2}}{L_{p,s}^2} \tau_{is,cab} \quad [\mathrm{s}] \quad \text{for large } N_s. \tag{5.15}$$

Note that for $l_{cab,1} = l_{cab,2} = l_{cab}/2$ the characteristic time τ_{bi} is about a factor $(l_{cab}/L_{p,s})^2$ larger than $\tau_{is,cab}$.

The time constant is either limited by the effective strand resistivity (regime A) or by the lengths and the cross-contact resistance (regime B) as shown in Fig. 5.16 for a 26-strand straight cable with lengths of 22 m and 110 m (as an example). The horizontal lines show eq. 5.13 while the lines which are inversely proportional to R_c represent eq. 5.14. The bold curve shows the characteristic time $\tau_{bi,av}$ as a function of R_c in the case of a cable with $l_{cab,1} = 2$ m and $l_{cab,2} = 20$ m. If R_c is small, the BICCs decay before the end of the cable

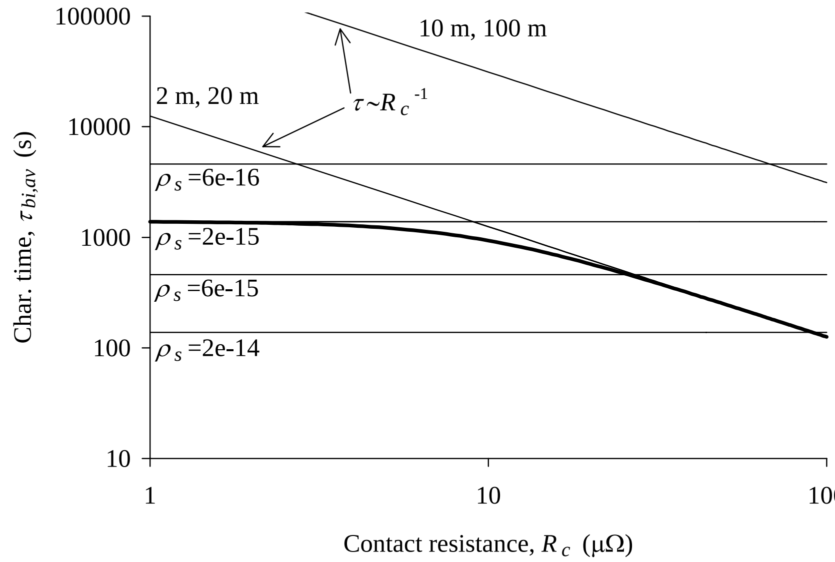

Figure 5.16. The characteristic time $\tau_{bi,av}$ as a function of the contact resistance R_c. The horizontal curves refer to regime A while the linearly decreasing curves represent regime B (where the two labels indicate the lengths $l_{cab,1}$ and $l_{cab,2}$). The bold line shows the actual characteristic time $\tau_{bi,av}$ in a cable with $l_{cab,1}=2$ m and $l_{cab,2}=20$ m ($N_s=26$, $d_s=1.3$ mm, $L_{p,s}=0.13$ m).

(regime A) so that $\tau_{bi,av}$ is independent of R_c (see eq. 5.13). If R_c is large, the characteristic time of the BICCs is limited by the lengths (regime B). The bold line deviates slightly for the region in-between regimes A and B. The above implies that similar coils with different R_c exhibit about the same $\tau_{bi,av}$ if the BICCs decay over a length ξ (regime A), while they exhibit different $\tau_{bi,av}$ if the BICCs decay over the whole cable (regime B).

The characteristic times of the BICCs in a coil can change (compared to a straight cable) due to the mutual inductances between the BICCs of the various turns. The interaction of the ISCCs between the turns of a stack of cable pieces causes an increase in the time constant of the ISCCs (see section 4.9) of about a factor 4-5 for LHC dipole magnets (see section 6.2.3) because the ISCC-distribution across the cable width is similar for each turn. However, the BICCs at a given strand position oscillate along the length with a phase that varies for each turn, since the length of each turn is different (see Fig. 2.3). Hence, $\tau_{bi,av}$ in a coil depends on the exact geometry of the coil, and can be a few times smaller or larger than $\tau_{bi,av}$ in a single straight cable. Of course, in an actual coil a spectrum of $\tau_{bi,av}$ is present due to the numerous $\dot{B}_\perp$-variations located at different positions with respect to the cable ends and possibly in sections with different R_c.

In section 3.4 it is shown that the IFCL can be expressed by $P_{if}=n\,\tau_{if}\,\dot{B}_{\perp s}{}^2/\mu_0$ with n a shape factor equal to 2 for strands with a round cross-section. A similar relation is shown to be present between P_c and $\tau_{is,cab}$ (see eq. 4.36). However, it is important to note that such a relation is *not* present between $\tau_{bi,av}$ and the enhancement of the ISCL due to the BICCs.

5.4.4 Propagation velocity of BICCs

In section 5.4.3, the characteristic time $\tau_{bi}(z)$ is defined as the time during which the BICCs at position z decay to 1/e of their initial values. As an example, $\tau_{bi}(z)$ is depicted in Fig. 5.17 for an 8-strand cable with $d_s = 1.3$ mm, $L_{p,s} = 0.1$ m, $R_c = 0.1$ μΩ and $\rho_s = 1.1 \cdot 10^{-14}$ Ωm (regime A).

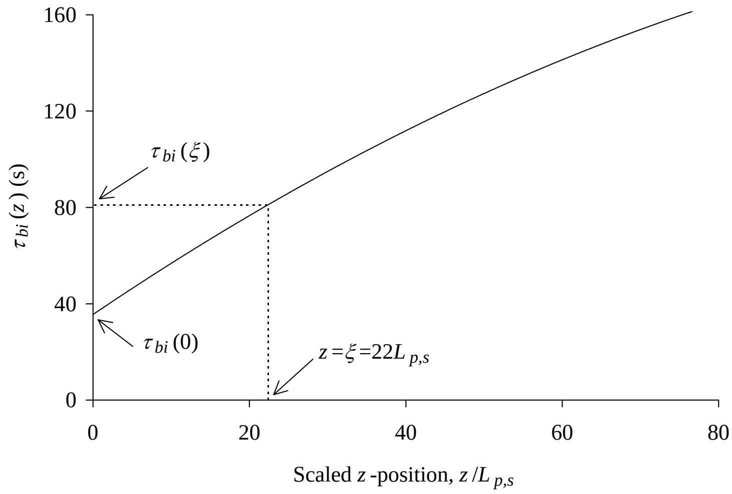

Figure 5.17. The time τ_{bi} at which the BICCs decay to 1/e of their initial values as a function of the z-position. The average propagation velocity $v_{bi,av}$ corresponds to the inverse of the slope of the curve between $z = 0$ and $z = \xi$.

The characteristic time can be expressed by:

$$\tau_{bi}(z) = \tau_{bi}(0) + \frac{z}{v_{bi}(z)} \quad [\text{s}] , \tag{5.16}$$

where $v_{bi}(z)$ is defined here as the propagation velocity of the BICCs through the cable which increases slightly with increasing z. In other words, the propagation velocity expresses the time it takes before a strand current at a certain distance from the $\dot{B}$ non-uniformity starts to change due to an additional BICC contribution (besides the transport current and the ISCC). The time dependent behaviour of the BICCs in a cable shows a certain similarity with electromagnetic waves that are characterised by a propagation velocity, and attenuation and dispersion along the length. In a coil the propagation velocity will probably be imperceptible since the BICCs caused by the numerous non-uniformities interfere and partially cancel. The increase in the characteristic time is, however, experimentally observed in a 1.3 m long cable (see section 5.8.3).

In the following an average velocity is defined over a length ξ (for regime A) and $l_{cab,i}/2$ (for regime B) as:

$$v_{bi,av} = \frac{\xi}{\tau_{bi}(\xi) - \tau_{bi}(0)} \quad [\text{ms}^{-1}] \quad \text{for regime A,} \tag{5.17}$$

and:

$$v_{bi,av} = \frac{l_{cab,i}/2}{\tau_{bi}(l_{cab,i}/2) - \tau_{bi}(0)} \quad [\mathrm{ms}^{-1}] \quad \text{for regime B,} \tag{5.18}$$

with $l_{cab,i} = l_{cab,1}$ for $z < 0$ and $l_{cab,i} = l_{cab,2}$ for $z \geq 0$.

The average propagation velocity is numerically calculated for regimes A and B and can be analytically described by the following formulas which are valid for $8 \leq N_s \leq 40$ with an error in the constants of proportionality of about 20%.

Regime A.

$$v_{bi,av} = 2.2 \cdot 10^7 \frac{\sqrt{R_c R_s}}{N_s} \quad [\mathrm{ms}^{-1}] \,, \tag{5.19}$$

which is equal to (using the expressions for ξ and $\tau_{bi,av}$ given by eqs. 5.7 and 5.13):

$$v_{bi,av} = \frac{\xi}{\tau_{bi,av}} \quad [\mathrm{ms}^{-1}] \,. \tag{5.20}$$

Combining eqs. 5.17 and 5.20 shows that $\tau_{bi}(\xi) = \tau_{bi,av} + \tau_{bi}(0) = 2.3\,\tau_{bi}(0)$ since $\tau_{bi,av} = 1.3\,\tau_{bi}(0)$ (see the remark after eq. 5.13), as can also be seen in Fig. 5.17.

Regime B.

$$v_{bi,av} = 1.7 \cdot 10^7 \frac{L_{p,s} R_c}{N_s^2 l_{cab,2}} \quad [\mathrm{ms}^{-1}] \quad \text{for } z \geq 0, \tag{5.21}$$

which can be combined with eq. 5.14 to give:

$$v_{bi,av} = \frac{l_{cab,1}}{\tau_{bi,av}} \quad [\mathrm{ms}^{-1}] \quad \text{for } z \geq 0. \tag{5.22}$$

In a similar way, $v_{bi,av}$ for $z < 0$ is equal to $l_{cab,2}/\tau_{bi,av}$.

5.4.5 Arbitrary $\dot{B}_\perp$-distributions

Due to the discrete nature of the cable, any distribution of $\dot{B}_\perp$ along the cable length can be modelled by a multi-step function, the value of which varies at each band (with a length of $L_{p,s}/N_s$) of the cable. Hence, there is a total of $N_B = l_{cab} N_s / L_{p,s}$ steps, where $z = 0$ corresponds to the end of the cable (i.e. $l_{cab,1} = 0$ and $l_{cab,2} = l_{cab}$). The multi-step function can be replaced by N_B single-step functions as long as the set of equations is completely linear, that is as long as ρ_s is independent of the current through the strand. The steady-state distribution of the BICCs can then be calculated as a summation of the BICCs of the N_B single-step functions, each with a field variation $\Delta\dot{B}_{\perp,m}$. According to eq. 5.4, the BICC in strand number i for regime A can be written as:

$$I_{bi,i}(z) = \sum_{m=0}^{N_B-1} I_{bi,0,m} \sin\left(2\pi(i-0.5+m)/N_s\right) e^{-\left|z-mL_{p,s}/N_s\right|/\xi} \quad [\mathrm{A}], \tag{5.23}$$

with (see eq. 5.5):

$$I_{bi,0,m} = 0.88\frac{w\xi}{R_c}\left(1-e^{-N_s/9.6}\right)\Delta\dot{B}_{\perp,m} \quad [\mathrm{A}]. \tag{5.24}$$

A similar expression can be derived for regime B by combining eqs. 5.9-5.11. An illustration is given in Fig. 5.18 for an 8-strand cable subject to a linear increase in $\dot{B}_\perp$ over a length l_t=5$L_{p,s}$/8. Only the single-step functions for which $\Delta\dot{B}_{\perp,m}\neq 0$ are shown.

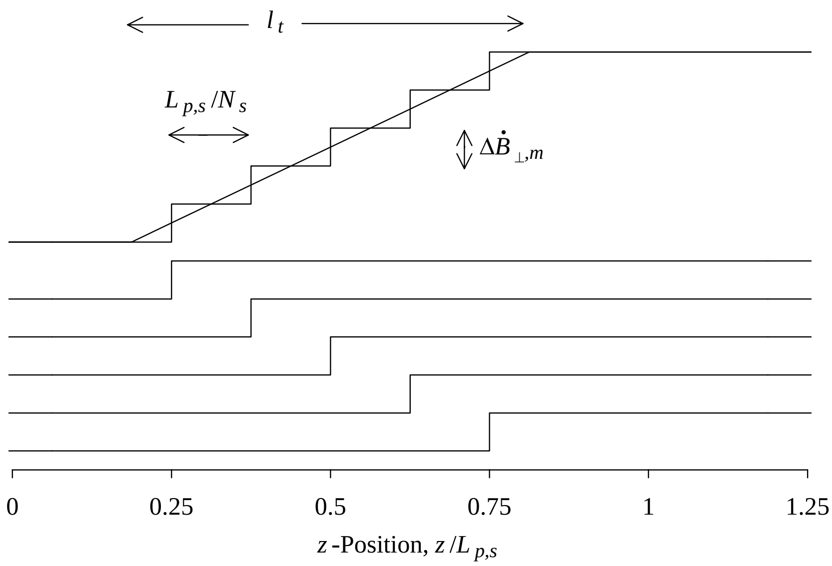

Figure 5.18. Representation of a linear increase in $\dot{B}_\perp$ by a multi-step function and consecutively by five single-step functions, shifted in the z-direction by a distance of one band length (=$L_{p,s}/N_s$).

Assuming l_t<<l_{cab} and ξ<<l_{cab} it can be easily seen that for regime A:

- The BICCs are maximum if the $\dot{B}_\perp$-transition happens in a single step, since the summation in eq. 5.23 can never be larger than $I_{bi,0}$ as defined by eq. 5.5. The largest magnitude of the BICCs for an arbitrary $\dot{B}_\perp$-variation is therefore directly given by eq. 5.5.
- The magnitudes of the BICCs depend on the length l_t. Minima are present for $l_t=k\cdot L_{p,s}$ with k=1, 2, 3, … and will be almost zero if ξ>>l_t. Maxima are present for $l_t=(k+0.5)\cdot L_{p,s}$ with k=0, 1, 2, … and decrease with increasing k.

Also the coupling power loss will have minima and maxima since the power is linear to the square of the coupling currents. The same conclusions hold for regime B, where the minima will be almost zero if $l_{cab,eff}$>>l_t.

It has been shown in section 5.1 that two types of $\dot{B}_\perp$-variations can be distinguished in a magnet:

- strong variations where $|\Delta\dot{B}_\perp/\Delta z|$ is of the same order as $|\dot{B}_{\perp,max}/L_{p,s}|$,
- weak variations where $|\Delta\dot{B}_\perp/\Delta z|$ is much smaller than $|\dot{B}_{\perp,max}/L_{p,s}|$.

According to eq. 5.24, an important conclusion is that the BICCs caused by strong variations are usually much larger than the BICCs caused by weak variations.

In a similar way it can be shown that a $\dot{B}_\perp$-dip over a width l_t, i.e.:

- $\dot{B}_\perp=\dot{B}_1$ for $z<0$,
- $\dot{B}_\perp=\dot{B}_2$ for $z>0$ and $z<l_t$,
- $\dot{B}_\perp=\dot{B}_1$ for $z>l_t$,

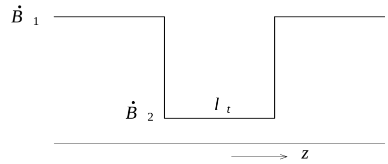

will also result in a minimum of the power loss for $l_t=k\cdot L_{p,s}$ with $k=1, 2, 3, \ldots$ and a maximum for $l_t=(k+0.5)\cdot L_{p,s}$ with $k=0, 1, 2, \ldots$

5.5 Cables that are partially exposed to $\dot{B}_\perp$

In the previous sections it is shown that BICCs are present in a cable which is exposed to a varying $\dot{B}_\perp$ in the z-direction. The magnitude of the BICCs varies along the length due to currents through R_c, which results in an additional loss, also in those parts of the cable where $\dot{B}_\perp$ is equal to 0. The enhancement of the ISCL due to BICCs is dealt with in this section for a cable with length l_{cab} which is locally subjected to $\dot{B}_\perp$ over a length l_a (see Fig. 5.19) centred along the cable.

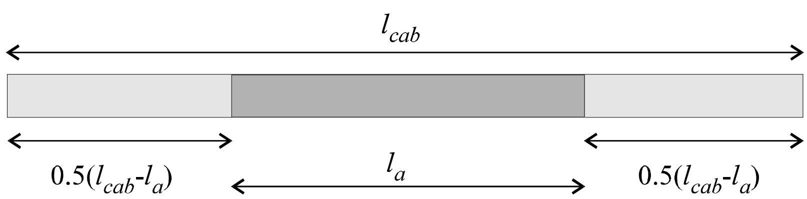

Figure 5.19. Illustration of a cable with length l_{cab} that is exposed to a varying magnetic field $\dot{B}_\perp$ over a length l_a located in the axial centre of the cable.

The typical enhancement of the ISCL in the case of a very small strand resistivity (regime B) is investigated as a function of:

- the length l_a for a constant cable length $l_{cab}=2$ m (case I, see Fig. 5.20),
- the cable length l_{cab} for a constant length $l_a=2.5L_{p,s}$ (case II, see Fig. 5.21),

with $N_s=16$, $L_{p,s}=0.1$ m, $w=8$ mm, $R_a=100$ μΩ, $R_c=1$ μΩ, $\rho_s=2.5\cdot10^{-18}$ Ωm, $\dot{B}_\perp=0.01$ Ts^{-1}.

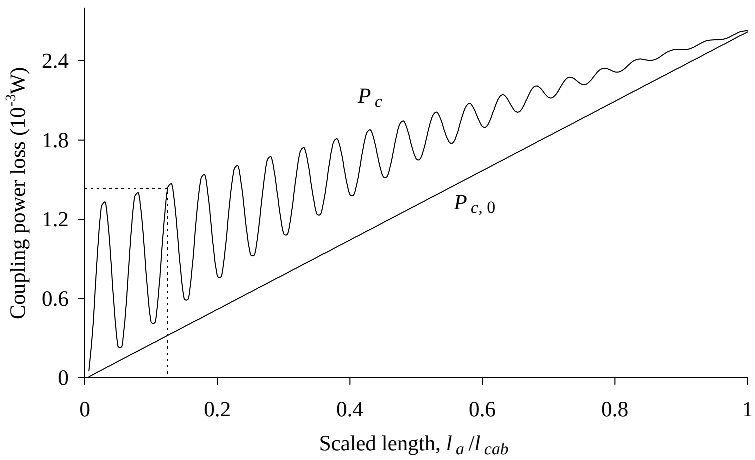

Figure 5.20. The coupling power loss in a cable with length $l_{cab} = 2$ m exposed to a locally applied $\dot{B}_\perp$ of length $0 < l_a < 2$ m. The dotted line shows the power loss for $l_a = 0.25$ m and corresponds to the value as given in Fig. 5.21.

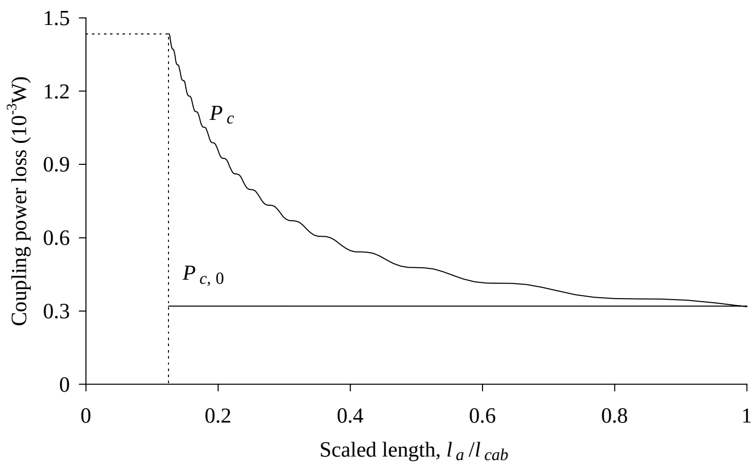

Figure 5.21. The coupling power loss in a cable with length l_{cab} exposed to a locally applied $\dot{B}_\perp$ of length $l_a = 0.25$ m. The cable length is varied between 0.25 m and 2 m. The dotted line shows the value for $l_{cab} = 2$ m and corresponds to the value as given in Fig. 5.20.

The power loss $P_{c,0}$ is equal to the power loss if no BICCs are present and is calculated using eq. 4.17, multiplied by l_a. The dotted lines in both figures correspond to the same case namely $l_a = 0.25$ m $= 2.5L_{p,s}$ and $l_{cab} = 2$ m $= 20L_{p,s}$.

The maxima in the power loss of Fig. 5.20 correspond to $l_a = (k + 0.5)L_{p,s}$ (see also section 5.4.5). The ISCL at the minima ($l_a = k \cdot L_{p,s}$) is larger than $P_{c,0}$ since the BICCs of the two $\dot{B}_\perp$-steps do not completely cancel due to the longitudinal decrease of the BICCs. The total loss in the cable increases significantly, especially for small l_a compared to l_{cab}.

The maxima will be less pronounced if the characteristic length of the BICCs is much smaller than l_{cab} (regime A).

The relative increase of the ISCL, $P_c/P_{c,0}$, for case I varies between two limits as can be seen in Fig. 5.20. The upper limit is given by the maxima in P_c, i.e. at $l_a=(k+0.5)L_{p,s}$ whereas the lower limit corresponds to $l_a=k{\cdot}L_{p,s}$. The relative increase of the ISCL for case II gradually decreases for increasing ratio l_a/l_{cab}. The scaled ISCL is depicted in both cases in Fig. 5.22.

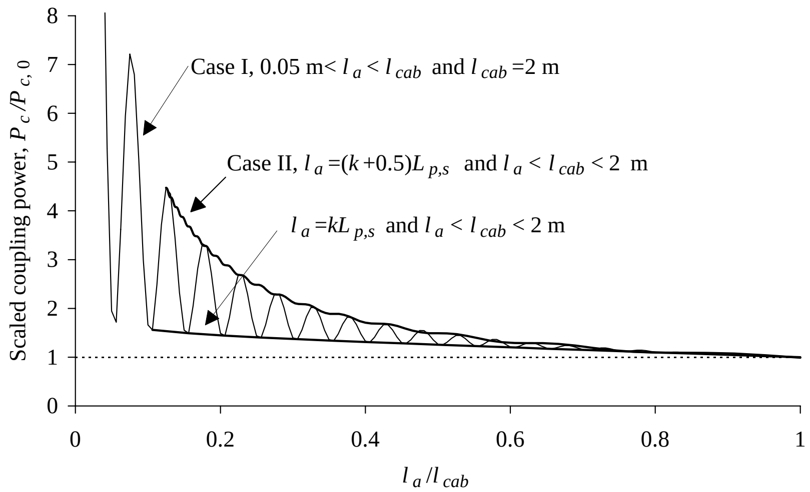

Figure 5.22. The relative enhancement of the ISCL in a cable that is locally exposed to $\dot{B}_\perp$ over a length l_a. Case I: $l_{cab}=2$ m, $0.05l_{cab}<l_a<l_{cab}$. Case II: $l_a=2.5L_{p,s}=0.25$ m, $l_a<l_{cab}<2$ m. The lower bold line shows also the case $l_a=2L_{p,s}=0.2$ m, $l_a<l_{cab}<2$ m.

An important conclusion is that a loss measurement on a cable with $l_a<l_{cab}$ will not result in a representative ISCL, and hence R_c. The enhancement of the ISCL depends on the ratio between l_a and l_{cab} and on the magnitude of the BICCs. The difference will be negligible if the strand resistivity is large so that $\xi<l_a$. To determine the representative loss of a long cable, the loss that is locally dissipated at the cable part of length l_a has to be measured by means of magnetisation or calorimetric measurements where the pick-up coils and the bell jar (which collects the evaporated helium) respectively cover only the length l_a of the cable.

In a dipole magnet the increase in the ISCL due to the BICCs cannot be calculated using the above figures since the $\dot{B}_\perp$-distribution is very complicated. However, a simple analysis shows that the increase is small since the local $\dot{B}_\perp$-dips are relatively small compared to the cable length (see Fig. 5.1). For example, in the case of a 1 m long LHC-type dipole the ratio l_a/l_{cab} is about 0.99 for each $\dot{B}_\perp$-dip. The total length of the $\dot{B}_\perp$-dips is about 20% of the cable length and thus $l_a/l_{cab}=0.8$. According to Fig. 5.22 the enhancement of the ISCL will then be about 10% maximum, but will be smaller in practical coils since the BICCs generated by the various $\dot{B}_\perp$-dips will partially cancel. Calculations with the network model in which the whole $\dot{B}_\perp$-distribution is incorporated shows that the increase is smaller than 5% and 1% for dipole magnets with lengths of 1 m and 10 m respectively.

5.6 $\dot{B}_\perp$-steps with R_c>>R_a

It is shown in section 5.4 that the magnitude of the BICCs can be reduced by increasing R_c where it is assumed that $R_a >> R_c$. However, for large R_c (for example by placing a resistive barrier between the two layers of the cable) some BICCs are still generated due to the presence of the adjacent resistances R_a. The following relations describe the characteristic length and magnitude for regimes A and B deduced from numerical simulations and are valid for $8 \le N_s \le 40$. The errors are about 10% for all the fitting constants.

Regime A.

Eq. 5.4 describes the *z*-dependence of the BICCs with the following new expressions for $I_{bi,0}$ and ξ:

$$I_{bi,0} = 0.45 \frac{w L_{p,s}}{N_s \sqrt{R_a R_s N_s}} \Delta \dot{B}_\perp \quad [\mathrm{A}] \,, \tag{5.25}$$

and:

$$\xi = 0.058 \sqrt{\frac{R_a}{R_s}} N_s^{0.13} \quad [\mathrm{m}] \,. \tag{5.26}$$

Note that these relations are qualitatively quite different from eqs. 5.5 and 5.7 since R_a and R_c have, of course, a very different effect on the current distribution in the cable. Combining eqs. 5.5, 5.7 and 5.25 shows that the magnitude $I_{bi,0}$ if $R_c << R_a$ is a factor F larger than the magnitude if $R_c >> R_a$ with:

$$F = 1.0 \sqrt{\frac{R_a N_s}{R_c}} \left(1 - e^{-N_s/9.6}\right) \approx \sqrt{\frac{R_a N_s}{R_c}} \quad \text{for large } N_s. \tag{5.27}$$

Regime B.

Eq. 5.9 describes the *z*-dependence of the linearly decaying BICCs with:

$$I_{bi,0} = 2.2 \frac{w l_{cab,eff}}{R_a N_s} \Delta \dot{B}_\perp \quad [\mathrm{A}] \,. \tag{5.28}$$

The factor F as defined above is equal to (combining eqs. 5.10 and 5.28):

$$F = 0.46 \frac{R_a N_s \left(1 - e^{-N_s/9.6}\right)}{R_c} \,. \tag{5.29}$$

The two values of F clearly show that a resistive barrier between the two layers of the cable strongly reduces the BICCs, especially for cables with a large number of strands. Assume, for example, a 30-strand cable with $R_a = 10$ μΩ, $R_c = 1$ μΩ. Inserting a resistive barrier and soldering the cable could result in $R_a = 1$ μΩ and $R_c >> R_a$. The magnitude of the BICCs will then decrease by a factor $F = 5.5$ (regime A) to 14 (regime B).

A local decrease in R_c (for example in a cable-to-cable connection) does not change the magnitude of the BICCs significantly (for a characteristic case of $R_a = 1$ μΩ and $R_c = 100$ μΩ and 0.5 μΩ in the connection).

5.7 Non-uniform R_c-distributions

In accelerator magnets R_c is likely to change across the cable width due to the keystone angle and the gradient in the transverse stress. This variation, however, does not generate BICCs as long as the variation is constant along the cable length. Longitudinal R_c-variations can be present along the whole cable of a pole, in the soldered connections, in local 'shorts' between strands and in the coil ends (see also section 5.1).

Each longitudinal variation in R_c generates BICCs with a characteristic length, a characteristic time, a propagation velocity and a magnitude in a similar way to that with a non-uniform $\dot{B}_\perp$.

The magnitude of the BICCs is investigated for a cable with a change in R_c along the cable length from $R_c = R_{c,1}$ for $z < 0$ to $R_c = R_{c,2}$ for $z \geq 0$. Fig. 5.23 shows the current in the strand at position 1 (see Fig. 5.5) along the length of the cable for $R_{c,1} = 1.5$ μΩ and $R_{c,2} = 0.5$ μΩ ($N_s = 16$, $d_s = 1.3$ mm, $I_{tr,str} = 0$ A, $\rho_s = 2 \cdot 10^{-14}$ Ωm, $\dot{B}_\perp = 0.01$ Ts^{-1}).

Note the similarity of the current pattern compared to Fig. 5.8. The average strand currents at the edge are about -4.5 A for $z < 0$ and -13.5 A for $z \geq 0$ and correspond to the ISCCs for a cable without longitudinal variations. Just as in the case of a step in $\dot{B}_\perp$, the BICCs can be regarded as currents that are maximum close to the R_c non-uniformity and decay quasi-exponentially (regime A) or quasi-linearly (regime B) towards 0.

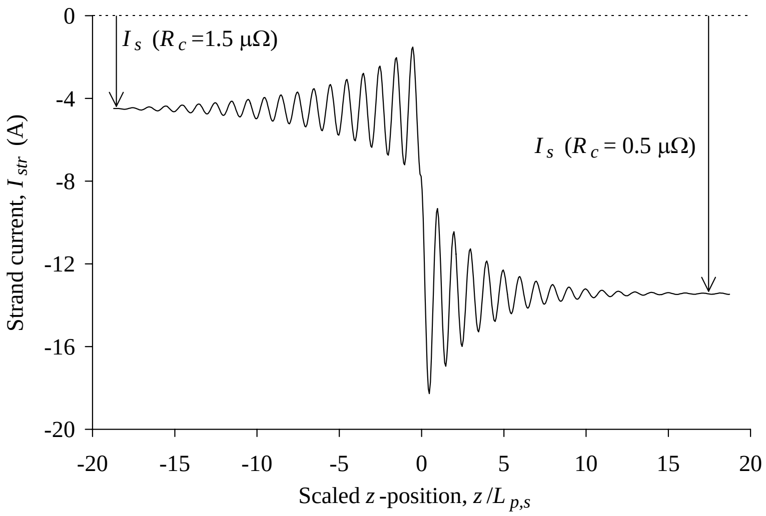

Figure 5.23. The characteristic pattern of the strand current at *position* 1 of a cable with a change in R_c from $R_{c,1} = 1.5$ μΩ for $z < 0$ to $R_{c,2} = 0.5$ μΩ for $z \geq 0$. The cable is subject to a field change of 0.01 Ts^{-1} (Regime A: $\rho_s = 2 \cdot 10^{-14}$ Ωm).

Regime A.

The characteristic length is different for $z<0$ and $z\geq 0$. The two characteristic lengths ξ_1 and ξ_2 are given by eq. 5.7 where R_c should be replaced by $R_{c,1}$ and $R_{c,2}$ respectively. For $8\leq N_s\leq 40$, the decay of the BICCs along the length is given by eq. 5.4 with $\xi=\xi_1$ for $z<0$ and $\xi=\xi_2$ for $z\geq 0$ and:

$$I_{bi,0} = 1.1\frac{wN_s}{R_{c,eff}}\xi_{eff}\sqrt{\frac{R_s}{R_{c,i}}}\left(1-e^{-N_s/9.6}\right)\dot{B}_\perp \quad [\mathrm{A}]\,, \tag{5.30}$$

with $R_{c,i}=R_{c,1}$ for $z<0$ and $R_{c,i}=R_{c,2}$ for $z\geq 0$,

$$\frac{1}{R_{c,eff}} = \left|\frac{1}{R_{c,1}} - \frac{1}{R_{c,2}}\right| \quad [\Omega^{-1}]\,, \tag{5.31}$$

and:

$$\xi_{eff} = \frac{\xi_1\xi_2}{\xi_1+\xi_2} \quad [\mathrm{m}]\,. \tag{5.32}$$

The error in the fitting constant 1.1 is smaller than 10%.

Regime B.

The more complicated relations of $I_{b,0}$ for regime B are disregarded here as well as the expressions for $\tau_{bi,av}$ and $v_{bi,av}$ for the two regimes.

BICCs due to a longitudinal R_c-variation are only generated if, at the place of the R_c-variation, the cable is exposed to a varying field $\dot{B}_\perp$. This implies that the R_c-variations in the splices and near the coil ends result in BICCs that are much larger than the BICCs caused by R_c-variations in the pole-to-pole connections and the connections between the cable and the current lead (which are located outside the high-field region of the coil).

In section 5.4.5 it is shown that an arbitrary $\dot{B}_\perp$-variation can be regarded as a finite summation of $\dot{B}_\perp$-steps. In a similar way the BICCs for an arbitrary R_c-distribution can be calculated by a summation of steps in $\xi_{eff}/R_{c,eff}$. Random distributions of R_c will not lead to considerable BICCs since the BICCs produced by all the small steps will mainly cancel. Cable sections where the average R_c is likely to differ, such as the coil ends and the splices, can be well simulated by two R_c-steps.

The magnitude of the BICCs provoked by an R_c-step and a $\dot{B}_\perp$-step is investigated by means of the characteristic case of the coil ends of a dipole magnet. This clarifies whether R_c- or $\dot{B}_\perp$-variations are the dominant source of BICCs. In the coil ends, the $\dot{B}_\perp$-variation is large since the cable bends around the beam pipe, and R_c is probably large since the strands are in weak contact. Here the $\dot{B}_\perp$- and the R_c-variations are assumed to be step-like.

The following parameters are taken for the characteristic case of a PBD magnet as specified in Table 2.1: $N_s = 26$, $w = 0.017$ m, $L_{p,s} = 0.1$ m, $d_s = 1.3$ mm, $\Delta\dot{B}_\perp = \dot{B}_\perp$ (see Fig. 5.1). The resistance $R_{c,end}$ in the ends is assumed to be much larger than the resistance R_c in the straight part so that $R_{c,eff} = R_c$. Combining eqs. 5.5 and 5.30, the ratio F between $I_{bi,0}$ in the case of a $\dot{B}_\perp$-step and an R_c-step is approximately:

$$F = \frac{I_{bi,0}^{\dot{B}\text{-}step}}{I_{bi,0}^{R_c\text{-}step}} = \frac{8 \cdot 10^{-7}}{\sqrt{\rho_s}} \quad , \tag{5.33}$$

which is much larger than 1 provided that ρ_s is smaller than 10^{-14} Ωm.

In section 7.7.5 the effective strand resistivity is estimated to be smaller than a few times 10^{-14} Ωm. An important conclusion is, therefore, that the BICCs in superconducting coils are mainly caused by $\dot{B}_\perp$-variations whereas R_c-variations only have a minor effect.

5.8 Experimental observation of BICCs in a 1.3 m long cable

5.8.1 Introduction

In sections 5.4.1-5.4.5 expressions are given for the characteristic lengths and magnitudes of BICCs in a straight cable. The formulas are derived for single $\dot{B}_\perp$- and R_c-steps and it is shown how more complex $\dot{B}_\perp$- and R_c-distributions can be dealt with. The major problem in estimating the BICCs in a coil is related to the partial cancelling of the BICCs produced by the numerous non-uniformities. Also the unknown effective strand resistivity prevents a good quantitative estimate of the BICCs. The characterisation of BICCs in magnets, by means of measurements of the magnetic field in the aperture of a magnet (see chapter 7), can therefore hardly be used to validate the formulas as derived in the previous sections.

In order to prove the existence of BICCs and to validate the formulas a new experimental set-up has been designed and constructed by which several parameters that affect the characteristics of the BICCs can be varied independently. It is based upon the measurement of the magnetic field, caused by the BICCs, along the length of a single straight cable. The cable can be locally subjected to a $\dot{B}_\perp$-variation and the R_c of the cable can be spatially changed. A description of the set-up and the features that can be implemented are given in section 5.8.2.

A discussion of the experimental results is presented in section 5.8.3. The field caused by the BICCs, the characteristic time, the propagation velocity and the decay pattern are analysed as a function of the field-sweep rate for several R_c-distributions. The results are compared to the numerically calculated formulas in order to validate the network model for modelling BICCs. The main purpose is to obtain a good qualitative agreement between the measurements and the calculations, whereas a good quantitative agreement is probably not possible since the exact spatial distribution of R_c is not well-known.

5.8.2 Experimental set-up

The test set-up has been designed in such a way that the characteristics of the BICCs, i.e.:

- the magnitude,
- the characteristic time,
- the propagation velocity,
- the decay along the length,

can be investigated for various spatial distributions of R_c and $\dot{B}_\perp$.

The schematic front view and cross-section are shown in Fig. 5.24. The set-up is installed vertically in a cryostat and immersed in liquid helium at 4.2 K. A keystoned Rutherford-type cable (cable I-1, see Table 2.4) with a length of 1.3 m (which corresponds to $10L_{p,s}$) is clamped over a length of 1.1 m ($=8.5L_{p,s}$) between two pressure bars. A transverse pressure on the cable of 15 MPa maximum can be applied by means of 30 bolts. The R_c-value can therefore be easily varied along the cable length. The strands in the two end sections of the cable, with a length of 10 cm, are in loose contact but can be soldered together to simulate the influence of the joint resistances on the characteristics of the BICCs.

A stainless-steel heater is fixed on the large faces of the cable in order to drive the cable from the superconducting into the normal state. The heater is electrically insulated from the pressure bar and the cable.

The field in the y-direction is determined by an array of eight Hall probes, each having an active area of about 1 mm^2. The centre of the probes is located at a distance of 2 mm from the narrow side of the cable. The probes are fixed on a small sledge which can move in the longitudinal direction over two glass guiding rods. The z-position of the sledge can be adjusted from outside the cryostat by means of a positioning bar with an accuracy better than 0.2 mm.

Two strands of the cable are connected to a current supply in order to calibrate the Hall probes. Furthermore, it can be investigated whether the BICCs are affected by an additional transport current in one of the strands.

A transverse field of 1.4 T maximum can be applied by means of a set of superconducting coils, located on both sides of the cable. The centre of the magnet is located at $z=0$. The cable lengths on either side of the magnet centre are 19 cm ($=1.4L_{p,s}$) and 111 cm ($=8.5L_{p,s}$). The $\dot{B}_\perp$-distribution along the cable caused by the set of coils when ramped from 0 to 1.4 T in 10 s is shown in Fig. 5.25. In the following the $\dot{B}_\perp$-value refers to the maximum field-sweep rate at $z=0$.

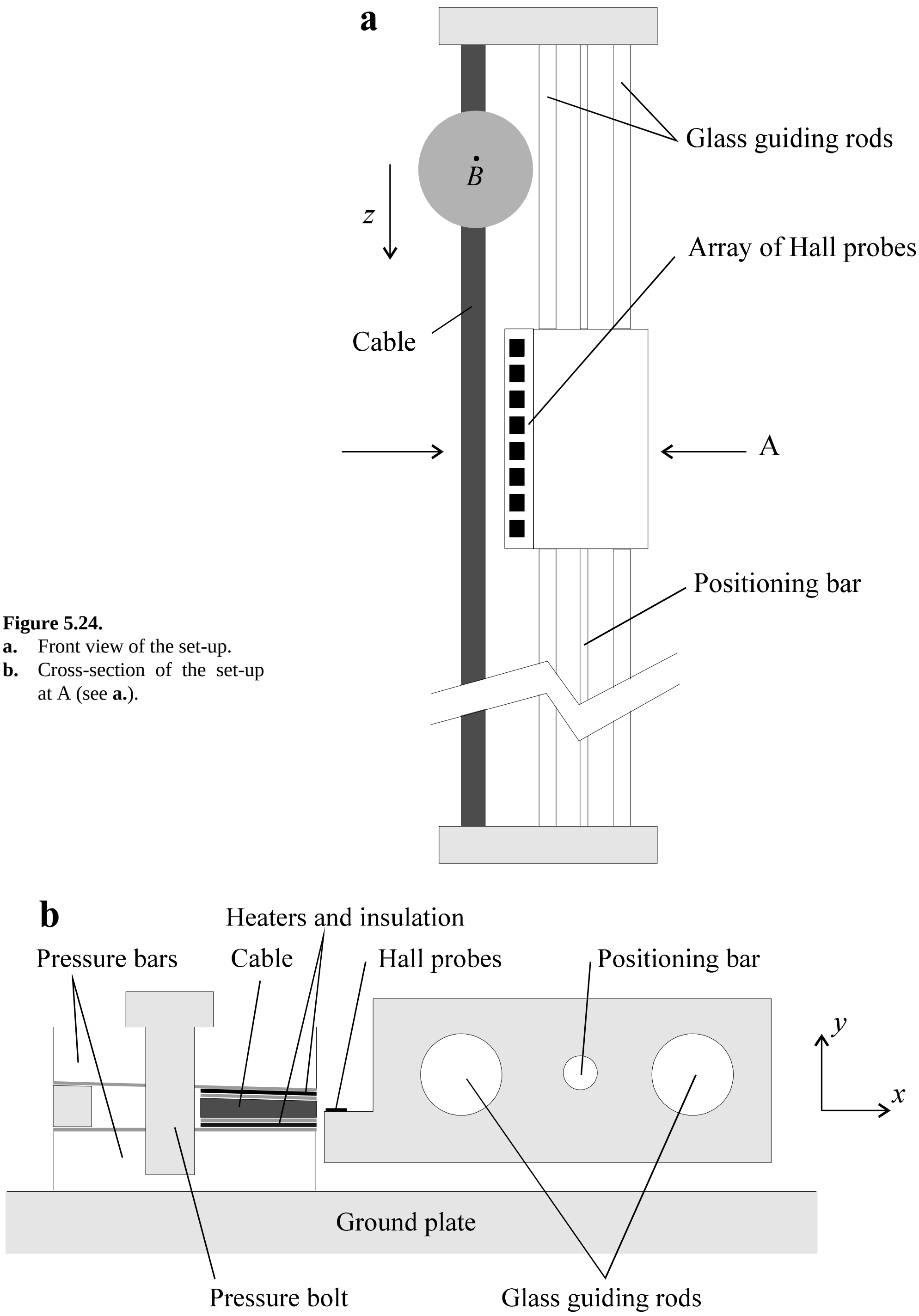

Figure 5.24.
a. Front view of the set-up.
b. Cross-section of the set-up at A (see **a.**).

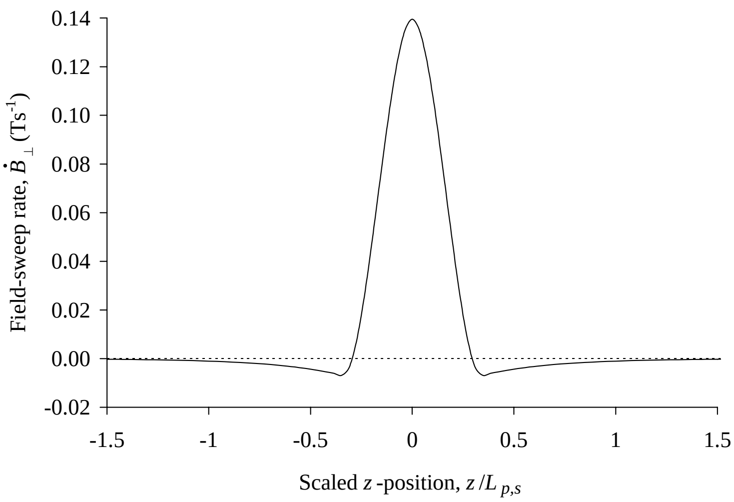

Figure 5.25. The applied field change $\dot{B}_\perp$ at the centre of the cable ($x = w/2$, see Fig. 4.1) along the cable length, for a field sweep of the set of coils from 0 to 1.4 T in 10 s.

The distribution of the contact resistance over the cable length can be, in first approximation, represented by five regions with contact resistances $R_{c,1}$ to $R_{c,5}$ (see Fig. 5.26). The contact resistance R_a is assumed to be larger than R_c and will be disregarded.

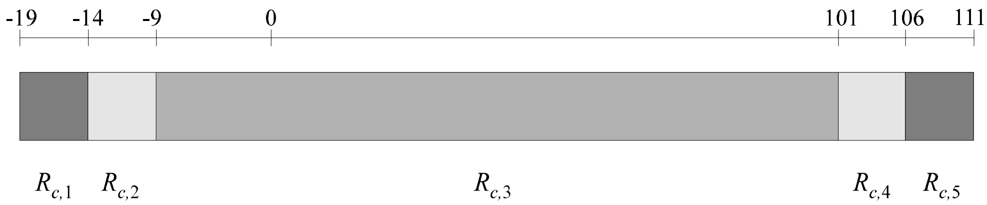

Figure 5.26. Approximation of the distribution of the cross-contact resistance along the cable length by means of five regions with different R_c. The z-position (in cm) is shown at the top.

The central part with a length of 110 cm covers the section which is pressurised at about 10-15 MPa. According to Fig. 4.29, $R_{c,3}$ is about 10-20 μΩ. However, due to the steep slope of the R_c-$P_\perp$ curve a significant larger value is possible for sections subject to a smaller pressure.

The end sections of the cable with a length of 10 cm have almost infinite R_c since the strands are in very poor contact with each other. Half of the end sections can be soldered, resulting in small $R_{c,1}$ and $R_{c,5}$. The R_c of a soldered cable is about 0.3 μΩ, according to Fig. 4.29. Since in the end sections a small gap is present between the strands of both layers of the cable, R_c is estimated to be a few times larger.

5.8.3 Results and discussion

The magnitude of the steady-state BICCs for the given $\dot{B}_{\perp}$- and R_c-distributions are calculated by means of the network model. The simulations are performed for a cable with the same geometry and number of strands as the measured cable. The field caused by the BICCs is calculated using the approach as discussed in section 7.2. Calculations of the characteristic time and the propagation velocity for this cable with its specific $\dot{B}_{\perp}$- and R_c-variations are not performed. First estimates of the characteristic time and propagation velocity are made using the formulas given in sections 5.4.3 and 5.4.4 and are compared to the measured values.

The field B_{bi}, produced by the BICCs, and the characteristic time are determined as a function of the z-position in the range $0.5L_{p,s}<z<7.5L_{p,s}$. Measurements are performed for three different R_c-distributions along the cable length (see Fig. 5.26):

I: a cable with unsoldered ends, i.e. $R_{c,1}$, $R_{c,2}$, $R_{c,4}$ and $R_{c,5}$ are much larger than $R_{c,3}$,
II: a cable with one soldered end, i.e. $R_{c,1}$ is about 1 μΩ, whereas the other R_c-values remain unchanged,
III: a cable with two soldered ends, i.e. $R_{c,1}$ and $R_{c,5}$ are about 1 μΩ, whereas the other R_c-values remain unchanged.

The field measured by the Hall probes consists of:
- the stray field of the magnet,
- the field B_{is} produced by the ISCCs,
- the field B_{if} produced by the IFCCs,
- the field B_{bi} produced by the BICCs, and
- the field B_m due to the filament magnetisation caused by the stray field of the magnet and by the field produced by all the coupling currents.

Field B_{bi} can be quite easily distinguished from the other field contributions, because:
- the magnitudes of fields B_{is} and B_{if} are negligible compared to the magnitude of the field B_{bi},
- the stray field and the magnetisation due to the stray field can be determined using a very small field-sweep rate,
- the magnetisation due to the coupling currents is relatively small compared to the amplitude of field B_{bi} itself.

The characteristic fields B_{bi} as measured with the Hall probes are shown in Fig. 5.27 at a field sweep from 0 to 1.4 T with 0.019 Ts^{-1} for case II (a cable with one soldered end). The figure shows clearly that the fields B_{bi} approach their steady-state values during the ramp and decay with a characteristic time of about 10 s as soon as the the field-sweep is finished.

Since the characteristic times during and after the field sweep are equal, it can be concluded that the BICCs are not significantly affected by the dynamic resistivity of the strand, which is proportional to $\dot{B}_{\perp}$ (see eq. 5.3). Measurements at various field-sweep rates prove that the steady-state fields (and hence the BICCs) are proportional to $\dot{B}_{\perp}$ whereas the characteristic time is independent of $\dot{B}_{\perp}$. Both results agree with the calculations (see eqs. 5.5, 5.10, 5.13 and 5.14).

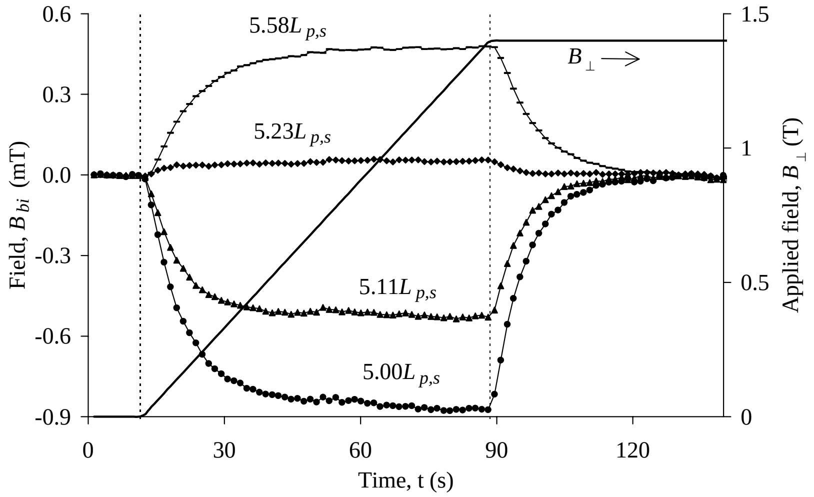

Figure 5.27. Field $\boldsymbol{B}_{bi}$ measured simultaneously by four Hall probes during and after a field sweep from 0 to 1.4 T (see the straight line) with $\dot{B}_{\perp}=0.019$ Ts^{-1}. The labels indicate the *z*-position of the Hall probe. The dotted lines show the start and the end of the field sweep.

The steady-state B_{bi}-values are measured along the cable for $0.5L_{p,s}<z<7.5L_{p,s}$ and depicted in Fig. 5.28 for case I with $\dot{B}_{\perp}=0.068$ Ts^{-1}. The continuous line corresponds to the calculated field using the network model with a finite and constant resistance $R_{c,3}$, infinite resistances $R_{c,1}$, $R_{c,2}$, $R_{c,4}$, $R_{c,5}$ and a very small strand resistivity, so that the BICCs can be classified in regime B (see section 5.4.1).

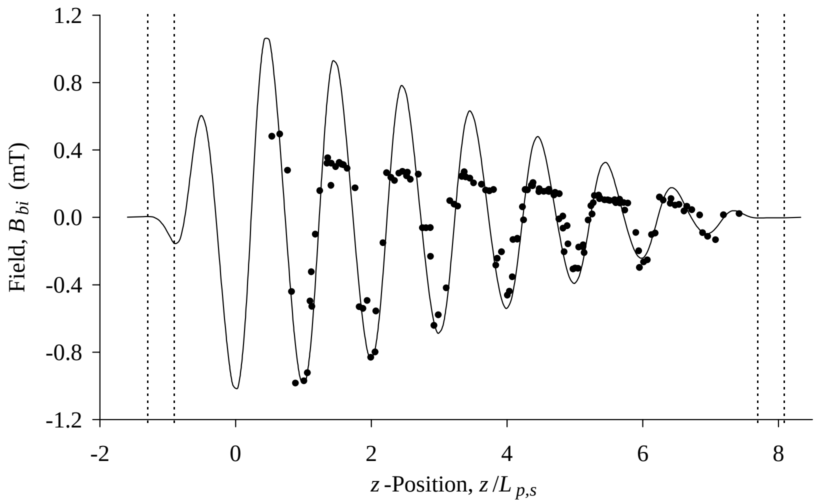

Figure 5.28. Field $\boldsymbol{B}_{bi}$ as a function of the *z*-position for case I with $\dot{B}_{\perp}=0.068$ Ts^{-1}. The dotted lines show the boundaries between the sections with different R_c (see Fig. 5.26). The continuous line corresponds to the calculated field using the network model.

The magnitude of the quasi-sinusoidally varying field, which depends in this case only on $R_{c,3}$, corresponds to the measured field assuming $R_{c,3}=100\ \mu\Omega$. This value is large compared to the expected value of 10-20 $\mu\Omega$, which could be caused by an overall decrease in the pressure on the cable (see Fig. 4.29), due to different shrinkage of the pressure bolts, the cable, the heaters and the insulation (see Fig. 5.24b) during cool-down. An increase in R_c near $z=0$ also results in significantly smaller BICCs even if R_c in the rest of the cable is much smaller.

The shape of the curve (with period $L_{p,s}$) does not depend on $R_{c,3}$ and corresponds very well with the measured one. Both the calculated curve and the measured points decay linearly to 0 at the end of the cable which prove that also the BICCs decay linearly to 0 (see also Fig. 5.9 as a comparison). The flattening in the maxima of the measured field is caused by one or a few strands that carry slightly smaller BICCs than expected. This is probably due to local variations in R_c, especially at $z<0$. Another possibility is that the surfaces of one or a few strands are more oxidised than the others or that some strands have a large effective strand resistivity. The linear decay imposes a certain maximum limit to the effective strand resistivity ρ_s. According to eq. 5.8, ρ_s should be smaller than a few times $10^{-13}\ \Omega$m. If it is larger, the characteristic length is smaller than 1 m which would result in a quasi-exponential decay.

Fig. 5.29 shows the characteristic time $\tau_{bi}(z)$ of the BICCs as a function of the z-position, determined from the decay of the field after a ramp from 1.4 T to 0 with $\dot{B}_\perp=-0.068\ \mathrm{Ts^{-1}}$. The time τ_{bi} at postion z is taken as the period during which the field B_{bi} at position z has decayed to 1/e of its steady-state value. The characteristic times are calculated for those positions which correspond to the maxima and minima in the field B_{bi} of Fig. 5.28.

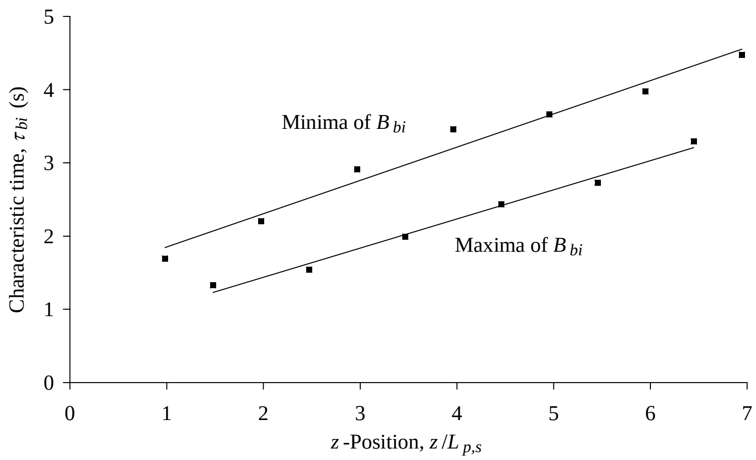

Figure 5.29. The characteristic time of the BICCs as a function of the z-position determined after a field sweep from 1.4 T to 0 with $\dot{B}_\perp=-0.068\ \mathrm{Ts^{-1}}$. The τ_{bi}-values are determined at those positions which correspond to the maxima and minima in B_{bi} of Fig. 5.28. The lines are linear fits.

Both curves are almost parallel, showing that the propagation velocity (see section 5.4.4) is more or less constant. The average time constant is slightly larger in the minima than in the maxima. This difference is directly related to the flattening in the curves of Fig. 5.28, since a flattening implies a larger series resistance in the BICC loop and hence a decrease of the characteristic time (see eq. 5.14).

It is interesting to investigate whether the formulas given in sections 5.4.3 and 5.4.4, which are valid in the case of a single $\dot{B}_\perp$-step, can also be applied to estimate the average characteristic time $\tau_{bi,av}$ and propagation velocity $v_{bi,av}$ for this cable exposed to the $\dot{B}_\perp$-distribution as shown in Fig. 5.25.

- The average time constant can be calculated using eq. 5.14 taking $R_c = 100\ \mu\Omega$, $l_{cab,1} = 0.09$ m, $l_{cab,2} = 1.01$ m, $N_s = 26$ and $L_{p,s} = 0.13$ m, which results in $\tau_{bi,av} = 0.3$ s. The estimated characteristic time is about a factor 7 smaller than the measured one (see Fig. 5.29 at about $z = 3L_{p,s}$).
- The average propagation velocity for $z \geq 0$ is estimated using eq. 5.21, which results in $v_{bi,av} = 1.7 \cdot 10^7 L_{p,s} R_c / (N_s^2 l_{cab,2}) = 0.3\ \mathrm{ms}^{-1}$. This value corresponds exactly to the experimentally obtained $v_{bi,av}$ as deduced from the average slope of Fig. 5.29: $v_{bi,av} = \Delta z / \Delta \tau_{bi} = 2.4 L_{p,s}\ \mathrm{s}^{-1} = 0.3\ \mathrm{ms}^{-1}$.

It can be concluded that the observed phenomena, i.e.:

– the *linear* decrease of the BICCs towards the end of the cable,
– the oscillation of B_{bi} with a *period* equal to $L_{p,s}$, and
– the presence of a characteristic time which increases almost *linearly* along the cable,

agree qualitatively very well with the calculations using the network model. Quantitative comparison of the average characteristic time and propagation velocity is difficult because the exact R_c-distribution over the length is not known and the formulas 5.14 and 5.21 are only valid for a $\dot{B}_\perp$-step.

In order to investigate the influence of sections with small R_c on the characteristics of BICCs, the R_c-distribution along the cable length is changed by soldering the ends of the cable with SnAg. Field B_{bi} is depicted in Figs. 5.30 and 5.31 for cases II (i.e. very small $R_{c,1}$) and III (i.e. very small $R_{c,1}$ and $R_{c,5}$).

The magnitude of B_{bi} increases strongly due to the local solderings, whereas the phase remains constant, in good agreement with the result from the network model. The calculated field, using the network model, can be fitted to the measurements by assuming a very small effective strand resistivity and taking:

– $R_{c,1} = 1.2\ \mu\Omega$ and $R_{c,3} = 100\ \mu\Omega$ (case II),
– $R_{c,1} = 1.2\ \mu\Omega$, $R_{c,3} = 100\ \mu\Omega$ and $R_{c,5} = 4\ \mu\Omega$ (case III).

A simple way to estimate $R_{c,5}$ is by considering the increase in the magnitude of the BICCs near $z = 0$ of case III compared to case II. Fig. 5.31 shows clearly that the increase is about a factor 2 (near $z = 0$) which implies that for $z > 0$ about half of the BICCs return through the resistances $R_{c,3}$ and the other half through $R_{c,5}$. Assuming a very small ρ_s, this implies that the equivalent resistance of the parallel $R_{c,3}$'s is about equal to that of the parallel $R_{c,5}$'s. Hence, $R_{c,3}/101 \approx R_{c,5}/5$ (see Fig. 5.26) or $R_{c,5} \approx 5\ \mu\Omega$ which agrees well with $R_{c,5}$ as obtained by the direct simulation using the network model.

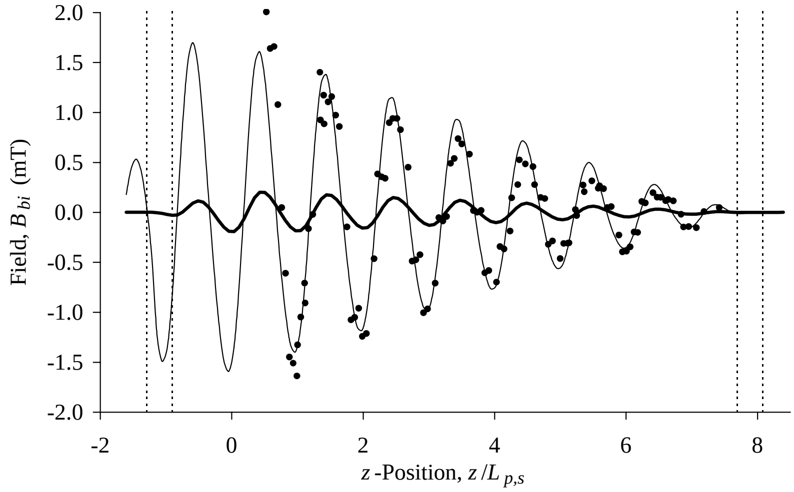

Figure 5.30. Field $\boldsymbol{B}_{bi}$ as a function of the z-position for case II with $\dot{B}_{\perp} = 0.016$ Ts^{-1}. The dotted lines show the boundaries between the sections with different R_c. The continuous lines correspond to the calculated field using the network model. The bold line shows the fitted curve of case I (see Fig. 5.28) scaled to $\dot{B}_{\perp} = 0.016$ Ts^{-1}.

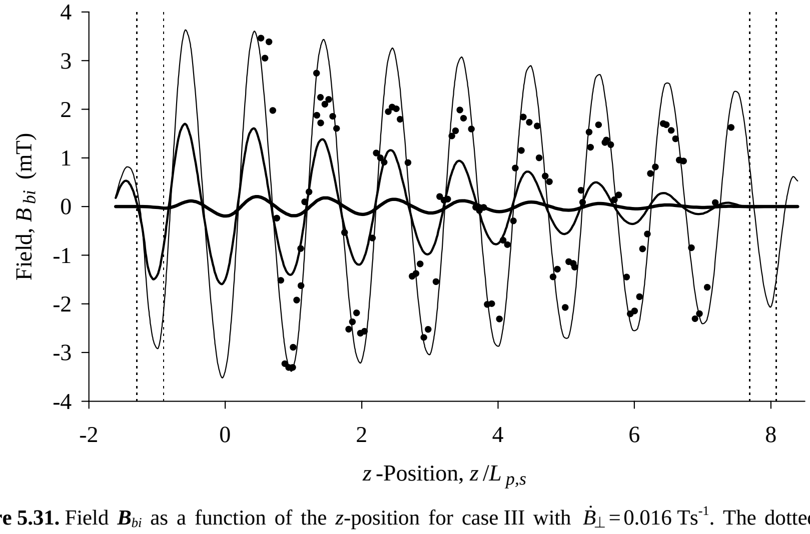

Figure 5.31. Field $\boldsymbol{B}_{bi}$ as a function of the z-position for case III with $\dot{B}_{\perp} = 0.016$ Ts^{-1}. The dotted lines show the boundaries between the sections with different R_c. The continuous line corresponds to the calculated field using the network model. The bold lines correspond to cases I and II (see Figs. 5.28 and 5.30) scaled to $\dot{B}_{\perp} = 0.016$ Ts^{-1}.

It can therefore be concluded that a local 'dip' in R_c influences the magnitude of the BICCs especially if the 'dip' is close to the $\dot{B}_{\perp}$ non-uniformity and if R_c is locally much smaller than the mean R_c of the cable. Consider, for example, the cable of a dipole coil with a mean

R_c equal to $R_{c,cab}$ and a joint with length l_{joint} and $R_c = R_{c,joint}$ located at a distance l_{diff} from the $\dot{B}_\perp$-variation. The joint will only significantly affect the magnitude of the BICCs (if classified in regime B) caused by the $\dot{B}_\perp$-variation if the distance l_{diff} is smaller than a few times $(R_{c,cab}/R_{c,joint})l_{joint}$.

If the BICCs are classified in regime A, the joint only affects the BICCs if the distance between the joint and the $\dot{B}_\perp$-variation is smaller than the characteristic length of the BICCs.

Note that the above discussion is valid for a joint located in a region with $\dot{B}_\perp = 0$. If, however, the joint is placed in a varying field, then additional BICCs will be induced (as discussed in section 5.7) caused by the R_c-step which is present at the boundary between the joint and the rest of the cable.

The characteristic times of cases II and III increase, compared to case I, by about a factor 4 and 10 respectively. Although no calculations are performed, the increase can be well understood by considering that the average loop length of the BICCs becomes larger while the series resistance in the loops (i.e., in first approximation, the equivalent resistance of the parallel R_c's) becomes smaller. The propagation velocity of the BICCs remains constant for $0.5L_{p,s} < z < 7.5L_{p,s}$. Simulations on small cables show a similar result, where the propagation velocity at position z is mainly determined by the local R_c at position z.

The large characteristic times of up to 30 s (for case III) show that very large $\tau_{bi,av}$-values of the order of 10^5 s may occur in magnets, with $R_c \approx 1\text{-}10\ \mu\Omega$ and a cable length much larger than 1 m, if the BICCs are classified in regime B (see also Fig. 5.16). This implies that the characteristic times of about 100 s which are measured in the aperture of the LHC dipole model magnets (see sections 7.7.1-7.7.5) have to be attributed to BICCs of regime A, decaying over much smaller lengths than the actual length of the cable in the magnet.

5.9 Conclusions

So-called Boundary-Induced Coupling Currents (BICCs) are generated in (Rutherford-type) cables, which are exposed to a varying field, if the field sweep rate or the contact resistances vary along the cable length.

BICCs differ from the 'normal' interstrand coupling currents because they stay in the strands over long distances of $10\text{-}10^3$ times the cable pitch (or the length of the cable). BICCs propagate through the cable and exhibit large characteristic times of $10\text{-}10^5$ s (for practical cables) which are several orders of magnitude larger than the time constant of the interstrand coupling currents.

The decay of the BICCs along the length of the cable is either quasi-exponential (regime A) or quasi-linear (regime B) (section 5.4.1). The type of decay is determined by the ratio between R_c and the effective strand resistivity. For large ratios the decay is quasi-linear towards 0 at the ends of the cable whereas for smaller ratios the BICCs decay exponentially towards 0 with a characteristic length. The slope of the decay varies according to the local R_c in the cable.

The BICCs are mainly caused by variations in the field change $\dot{B}_{\perp}$ transverse to the cable width, and their magnitude increases strongly if the lengths of the $\dot{B}_{\perp}$-variations are of the same order or smaller than the cable pitch (see section 5.4.5). In the case of a dipole magnet this implies that the field variations in the coil ends cause large BICCs whereas the gradual variation of $\dot{B}_{\perp}$ to which the total cable is exposed only causes relatively small BICCs.

In practical coils, the magnitude of the BICCs caused by $\dot{B}_{\perp}$-variations is much larger than the magnitude caused by R_c-variations (see section 5.7). This implies that the soldered cable-to-cable connections cause smaller BICCs than the $\dot{B}_{\perp}$-variations in the coil ends. However, local decreases in R_c (and hence also cable-to-cable connections) could significantly increase the magnitude and the characteristic time of the BICCs *caused by a* $\dot{B}_{\perp}$*-step*. This implies that also in cables having a large R_c, BICCs will be present if the cable is locally soldered (even if the soldered parts are located in a low-field region).

The presence of BICCs causes an additional power loss, also in those parts of the cable which are not subject to the varying field. The relative increase of the power loss is large compared to the ‘normal’ interstrand coupling loss if only a small part of the cable is exposed to a field variation (see section 5.5). In accelerator dipole and quadrupole magnets the enhancement of the power loss is smaller than 10% of the interstrand coupling loss.

The magnitude of the BICCs can be reduced by increasing the contact resistances R_a and especially R_c. Insertion of a resistive barrier in-between the two layers of a Rutherford-type cable (with originally R_a=R_c) can reduce the magnitude of the BICCs by about one order of magnitude (see section 5.6).

The existence of BICCs is experimentally demonstrated in a 1.3 m long Rutherford-type cable exposed to a small local field change. The characteristics of BICCs, such as the decay along the length, the decay as a function of the time and the propagation velocity are qualitatively in very good agreement with the results based on the network model. The influence of local soldering of the cable, simulating the cable-to-cable connections in a coil, on the characteristics of the BICCs corresponds to the network results as well. Quantitative differences of up to a factor of about 5 are probably caused by the unknown variations in R_c along the cable. The fact that the magnitude of BICCs in a single cable is already hard to assess shows that the BICCs in an entire coil will be even more complicated to calculate, especially if the spatial R_c-distribution is not well-known.

Large characteristic times of 10^4-10^5 s of the BICCs in accelerator dipole magnets (with R_c of the order of 1-10 μΩ) imply that the BICCs are classified in regime B and can attain large magnitudes if the ends of the cables are soldered, even if the strands in the rest of the cable are in poor electrical contact. BICCs exhibiting characteristic times of the order of 10^2-10^3 s have to be classified in regime A, and their magnitude is much less sensitive to R_c in the soldered ends of the cable. In a coil, a combination of these two regimes is present.

In dipole and quadrupole accelerator magnets the BICCs cause sinusoidally varying field distortions along the magnet axis with a large characteristic time, an amplitude proportional to the central-field-sweep rate and a period equal to the cable pitch. These field distortions will be discussed in detail in chapter 7. The effect of the BICCs on the stability of a coil is discussed in chapter 8.